International Journal of Nanomedicine Dovepress

Open Access Full Text Article ORIGINAL RESEARCH

A Graphene-Based Lipid Modulation Nanoplatform for Synergetic Lipid Starvation/ Chemo/Photothermal Therapy of Oral Squamous Cell Carcinoma

Ran Li[1,2,*], Yanwei Li[1,2,*], Zijian Song[1,2], Yixuan Gu[1,2], Xiaofeng Jiao[1,2], Chaoqiong Wan[1,2], Tiantian Liu[1,2], Rongrong Zhang[1,2], Ruifang Gao[1,2], Xiangyu Wang[1,2]

[1]Shanxi Province Key Laboratory of Oral Diseases Prevention and New Materials, Shanxi Medical University School and Hospital of Stomatology, Taiyuan, 030001, People's Republic of China; [2]Department of Pediatric and Preventive Dentistry, Shanxi Medical University School and Hospital of Stomatology, Taiyuan, 030001, People's Republic of China

*These authors contributed equally to this work

Correspondence: Ran Li; Xiangyu Wang, Email lraner@163.com; wangxiangyu76@163.com

Purpose: Chemotherapy is one of the most commonly used treatments for oral squamous cell carcinoma (OSCC), but its use is limited by drug resistance and severe systemic toxicity. To eliminate these side effects and improve anti-tumor efficacy, several therapeutic approaches have been developed for use with chemotherapy. In this study, we developed a graphene-based lipid modulation nanoplatform (NSD) that carries SB-204990, a small molecule inhibitor specific for ATP citrate lyase (ACLY), and doxorubicin (DOX), a chemotherapeutic agent, and the trio enables synergistic treatment of OSCC with lipid starvation, chemotherapy, and photothermal therapy.

Methods: We first determined whether ACLY expression was upregulated in OSCC, and then assessed the growth inhibitory effects of SB-204990 on SCC-15 cells and changes in lipid (acetyl coenzyme A, free fatty acids, and cholesterol) levels. We characterized NSD and then evaluated the stability, photothermal properties, drug loading, and release ability of NSD. Finally, the therapeutic effects of NSD on OSCC were investigated by in vitro and in vivo experiments, and the changes in lipid levels in OSCC tissues after ACLY inhibition were further evaluated.

Results: The results showed that ACLY was highly expressed in OSCC, and ACLY inhibition produced reproductive suppression and decreased lipid levels in SCC-15 cells. The NSD nanoplatform possessed good stability, photothermal properties, high drug loading capacity and controlled release. In addition, the triple therapy achieved satisfactory anticancer effects in both in vivo and in vitro assays, and the inhibition rate of tumors was as high as 99.4% in the NSD+Laser treatment group.

Conclusion: The changes in tumor cell lipid levels and cell proliferation arrest induced by ACLY inhibition suggest that ACLY may be a promising target for lipid starvation therapy and resistance to chemoresistance, and its inhibitors are expected to become new anticancer drugs. The NSD nanocarrier system enables synergistic treatment with lipid starvation, chemotherapy, and photothermal therapy, which represents an innovative approach to combating tumors.

Keywords: starvation therapy, ACLY, nanotechnology, chemotherapy resistance, OSCC

Introduction

Based on the most recent worldwide data, oral and lip cancers rank as the 16th most prevalent cancers worldwide, accounting for approximately 355,000 new cases annually.[1] Oral squamous cell carcinomas (OSCC) constitute over 90% of all oral cancer cases.[2] While conventional chemotherapy remains a widely used cancer treatment, drug resistance often leads to treatment failure.[3] The major drawbacks of systemic chemotherapy include low drug concentration at the tumor site, short retention time, and systemic toxicities.[4] Drug resistance refers to the ability of tumor cells to attenuate and

Received: 14 May 2024
Accepted: 17 October 2024
Published: 4 November 2024

Graphical Abstract

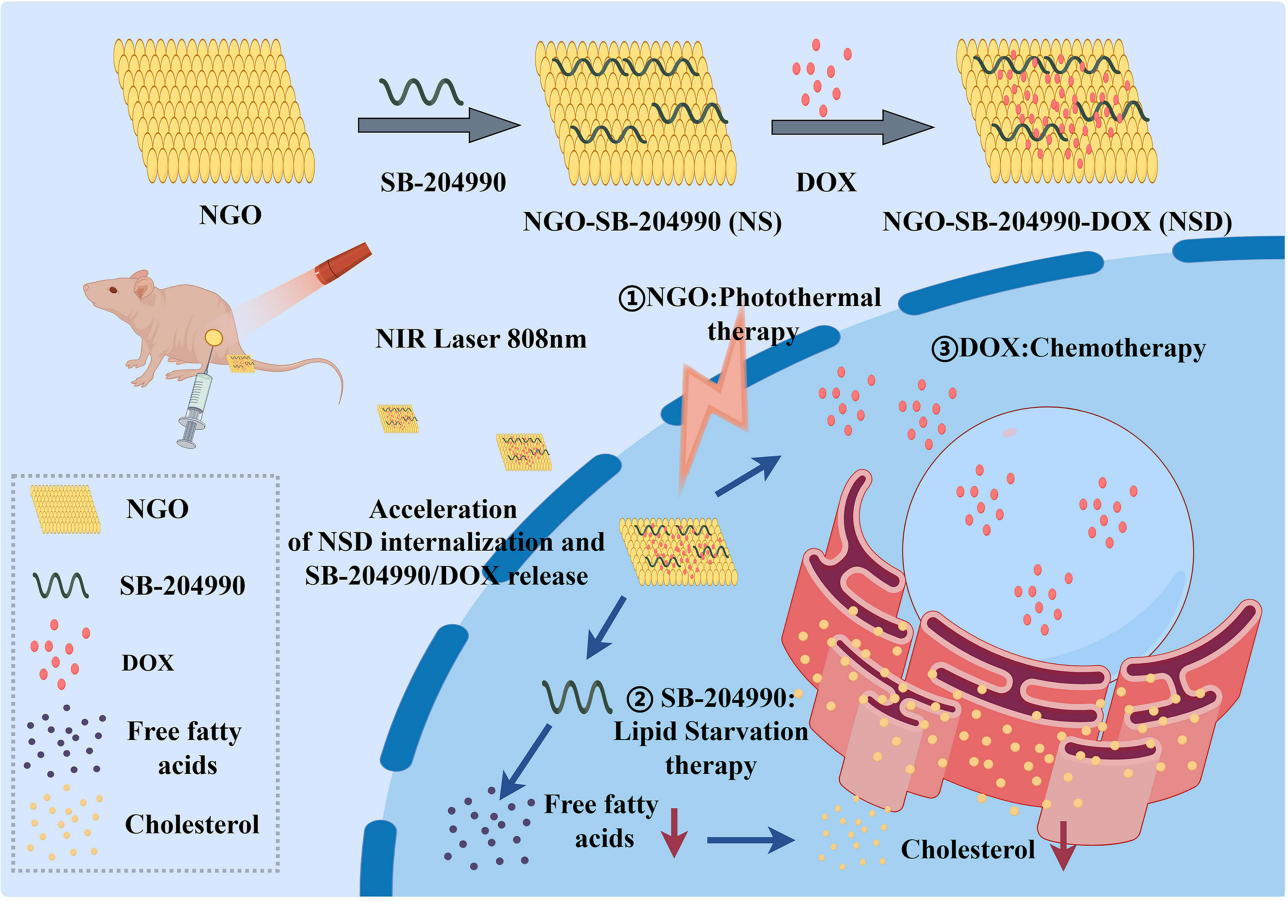

resist the cytotoxic or inhibitory effects of anticancer drugs through the production of multiple defense mechanisms, thereby reducing the therapeutic effect.[5] Tumors with intrinsic resistance show a resistant phenotype to chemotherapy before encountering the chemotherapeutic agent, whereas acquired-resistant tumors may initially respond to chemotherapy but then become insensitive to similar agents. But both intrinsic and acquired resistance are generated and maintained by reducing drug accumulation and increasing drug output, modifying drug targets, and signaling molecules, enhancing repair of drug-induced DNA damage, and avoiding apoptosis in tumor cells.[6] Various approaches have been reported to overcome drug resistance and eliminate systemic toxicity of chemotherapeutic agents.

Recent studies highlight the reprogramming of lipid metabolism as an important feature of cancer metabolism and that this metabolic alteration in cancer cells may contribute to chemoresistance.[7] Unlike normal cells, tumor cells tend to self-synthesize lipids.[8] Abnormal initiation of fatty acid (FA) and cholesterol biosynthesis equips tumor cells with components for biofilm formation, sustained energy, and signaling molecules.[9] This enables tumor cells to proliferate rapidly and adapt to various harsh tumor microenvironments, such as limited nutrient and oxygen availability. Cutting off the lipid metabolism of tumor cells will cause them to die of "nutrient starvation". Furthermore, reprogramming of lipid metabolism promotes disease progression and metastasis, alters the body's response to anticancer treatments, and ultimately leads to drug resistance.[10] It has been demonstrated that gefitinib-resistant cells in non-small cell lung cancer had considerably greater cholesterol levels than gefitinib-sensitive cells.[11] Furthermore, mesenchymal stem cells (MSCs) in gastric cancer can encourage tumor cell self-renewal and resistance to treatment through FAO (fatty acid oxidation). Etomoxiry, an FAO inhibitor, dramatically improved stem cell characteristics and oxaliplatin and 5-FU resistance.[12]

Therefore, inhibition of lipid metabolism in tumor cells will not only cause cell growth arrest, but may also restore the sensitivity of chemotherapeutic drugs, and abnormalities in lipid metabolism are expected to be a dual action target for both anticancer and drug resistance. Several anti-tumor strategies have emerged targeting key enzymes involved in lipid synthesis, uptake, and storage,[13] including ATP citrate lyase (ACLY), a central metabolic enzyme. ACLY, a cytoplasmic homotetrameric enzyme, hydrolyzes ATP to ADP and phosphate, concurrently catalyzing the conversion of citrate and coenzyme A (CoA) to acetyl coenzyme A and oxaloacetate.[14] Acetyl-coenzyme A plays a crucial role in the production of fatty acids, cholesterol, and isoprenoids.[15] Therefore, inhibiting ACLY may downregulate acetyl-CoA levels in tumor cells, leading to decreased fatty acid and cholesterol production. Fatty acid or cholesterol starvation, or both, may lead to reduced drug resistance and growth arrest in tumor cells with high ACLY expression mediated by ACLY knockdown.[16] ACLY expression is significantly upregulated in many types of cancers, such as hepatocellular carcinoma, colorectal cancer, breast cancer, glioblastoma, and non-small cell lung cancer, compared to normal cells.[17,18] However, there is insufficient evidence to demonstrate that ACLY expression is upregulated in OSCC. We plan to first verify whether ACLY is highly expressed in OSCC, and then use the ACLY-specific small molecule inhibitor, SB-204990, to act on tumor cells and explore its anticancer effects as well as the effects on tumor lipid levels to verify the potential of ACLY inhibition on improving chemotherapy resistance.

In addition to decreasing the lipid metabolism of tumor cells, thereby increasing anticancer effects and sensitivity to chemotherapeutic agents, photothermal therapy (PTT) is often used in combination with chemotherapy to increase the sensitivity of cancer cells to drugs by increasing the effective concentration of drugs in the cells.[19] In addition, under near-infrared (NIR) laser irradiation, photothermal agents can convert light energy into heat energy and induce apoptosis of tumor cells by increasing the local temperature of the tumor. Thus, photothermal therapy, like lipid-lowering therapy, may have the dual effect of fighting cancer and inhibiting chemotherapy resistance. Graphene, as a photothermal agent, not only possesses excellent photothermal properties but also has the characteristics of easy modification, high drug loading rate, and controlled drug release, which has been widely used in tumor photothermal therapy in recent years.[20,21] However, conventional graphene has poor water solubility and low bioavailability. The oxidized form of graphene, with hydrophilic groups on its surface including hydroxyl, carbonyl, carboxyl, and carboxylate functional groups, has been reported to increase water solubility, reduce toxicity, and greatly improve bioavailability.[22,23] On this basis, we used carboxylated graphene oxide (NGO) that introduced more carboxyl groups, which further increased the water solubility. In addition, more carboxyl groups allow drugs (eg small molecules, DNA, RNA, proteins) to bind extensively to the NGO via electrostatic, covalent, and hydrogen bonds, which strengthens the deliverability of the NGO as a drug carrier.[24,25] Therefore, NGO is a potential drug delivery carrier, which we have successfully tried in previous studies.

Doxorubicin (DOX) is an effective and commonly used fluorescent chemotherapeutic agent, but cardiotoxicity severely limits its application.[26,27] Nanodrug delivery systems not only enable efficient loading and release of drugs but also improve drug enrichment and utilization at the lesion site.[28] Currently, many studies use nanocarriers to deliver DOX, which can greatly reduce the dosage and thus its toxicity.[29,30] In this study, we used NGO to deliver SB-204990 and DOX together and then synthesized a new lipid-modulating nanoplatform NGO-SB-204990-DOX (NSD). In the first place, photothermal and low pH environments facilitate expedited extracellular uptake and intracellular release of the ACLY inhibitor SB-204990 and DOX, thereby elevating the intracellularly effective level of the drug while concurrently thwarting chemotherapeutic drug resistance alongside DOX. Secondly, the reversal of sorafenib resistance in hepatocellular carcinoma by targeted inhibition of ACLY expression has been reported,[31] but the efficacy of ACLY inhibition in combating chemoresistance in OSCC has not been explored. On this basis, we tried for the first time to ameliorate the low sensitivity of DOX in OSCC using the ACLY-specific small molecule inhibitor SB-204990. More importantly, photothermal therapy and lipid starvation therapy are cytotoxic in themselves and synergistic with chemotherapy. Therefore, all three act together on tumor cells, maximizing the anti-cancer effect. Since most of the nutrient starvation therapies discussed in the literature focus on glucose deprivation,[32] we term lipid-lowering starvation therapy as "lipid starvation therapy". Since the lipid alterations caused by ACLY inhibition are complicated, we will only be looking at three main markers in this article: acetyl coenzyme A, free fatty acids, and total cholesterol. The synergistic effect of NSD on OSCC has been validated in vitro and in animal models, underscoring the effectiveness of NSD multimodal antitumor therapy, which is a successful pioneer of synergistic treatment in combination with lipid starvation, chemotherapy, and photothermal therapy.

Materials and Methods

Chemicals

Ultrathin graphite was obtained from XFNANO (Nanjing, China), SB-204990 from MCE (Shanghai, China), DOX from Sigma-Aldrich (St. Louis, Missouri, USA), and modified Eagle's medium (DMEM) and fetal bovine serum (FBS) from Gibco (New York, USA). Trypsin, penicillin, and streptomycin were purchased from Meilunbio (Dalian, China). The Bicinchoninic acid (BCA) protein kit was purchased from Beyotime (Shanghai, China). Additionally, the Calcein-AM/PI Live/Dead Cell Staining Kit was purchased from BBcellProbe® (Zhengzhou, China), and the Annexin V-FITC/PI Apoptosis Detection Kit was obtained from Solarbio (Beijing, China). The CCK-8 Kit, Universal Acetyl Coenzyme A kit, Universal Free Fatty Acid kit, and Universal Total Cholesterol Assay kit were all purchased from Abcam (Cambridge, UK).

Cell Culture

Human HOK and SCC-15 cells were acquired from Pricella (Wuhan, China) and cultured in culture flasks with DMEM containing 1% penicillin, 1% streptomycin, and 10% (v/v) fetal bovine serum. The flasks were maintained in a humidified incubator with 5% CO_2 at 37 °C. Cells were collected in 15 mL tubes and centrifuged for 5 minutes at 1000 × g, with passaging conducted every 2–3 days. The supernatant was discarded and replaced with a fresh medium.

Hematoxylin and Eosin (HE) Staining and Immunohistochemistry

Tissue sections, 4 μm thick, were deparaffinized and rehydrated before staining for either immunohistochemistry or HE. Sections were sealed with 3% hydrogen peroxide and incubated with 10% goat serum for 30 minutes at room temperature. Subsequently, they were treated overnight at 4 °C with rabbit anti-ACLY monoclonal antibody. Specimens were subjected to color development using a DAB Color Development Kit (Solarbio, China). The human specimens for this experiment were obtained from the Stomatological Hospital of Shanxi Medical University, which included 58 cases of OSCC tissues and corresponding adjacent normal tissues. The Medical Ethics Committee of the Stomatological Hospital of Shanxi Medical University approved all experimental procedures, and all procedures followed the principles of the Declaration of Helsinki. All patients gave informed consent and underwent an ethical review. Relevant Ethics approval number: 2023LL038.

Quantitative Real-Time PCR

Cellular RNA was reverse transcribed using the ReverTra Ace® qPCR RT Kit (Solarbio, China) following the manufacturer's instructions. Quantitative real-time PCR analysis was performed using SYBR Green Real-time PCR Master Mix (Solarbio, China). Cycling parameters were set as follows: 95°C for 100 s, followed by 40 cycles of 95 °C for 15s, 60 °C for 15s, and 72 °C for 45s. The melting curve analysis was conducted with the following program: 95 °C for 15s, 60 °C for 60s, and 95 °C for 1s.

Primers used:

ACLY	F 5'-TCGGCCAAGGCAATTTCAGAG-3'
	R 5'-CGAGCATACTTGAACCGATTCT-3'
GAPDH	F 5'- GATTCCACCCATGGCAAATTC −3'
	R 5'- CTGGAAGATGGTGATGGGGATT-3'

Western Blotting

Total proteins were extracted from HOK and SCC-15 cells, and their concentrations were measured. Equal amounts of proteins (30 μg/lane) were separated by SDS-PAGE on 10% gels. Semi-dry transfer using a Bio-Rad transfer cell at 25 V for 30 min was employed to transfer cellular proteins onto PVDF membranes (Millipore, USA). After blocking with 5% skim milk and washing with TBST, membranes were incubated overnight at 4 °C with primary antibodies (ACLY antibody, Abcam,

UK, 1:1000 dilution; GAPDH antibody, MCE, China, 1:10,000 dilution). Subsequently, membranes were incubated with secondary antibodies coupled with horseradish peroxidase (HRP) for 1 h at room temperature. Immunoreactive proteins were visualized using enhanced chemiluminescence (ECL, Millipore) following the manufacturer's recommendations.

Wound-Healing and Transwell Chamber Migration Experiment

For wound healing experiments, cells were inoculated in 6-well plates and scraped with a sterile 0.2 mL pipette tip. Cultured in medium containing 20% FBS and photographed at different time points. Images were obtained using a microscope.

For transwell migration experiments, cells were inoculated in the top chamber of the transwell, serum-free DMEM medium was added to the top chamber, and DMEM containing 20% FBS was added to the basal side chamber of the transwell. After 48 h of incubation, the cells were fixed with 4% paraformaldehyde (PFA) and stained with crystal violet.

Preparation of NGO

Graphene oxide was produced by modifying the Hummer process from natural graphite. First, deionized (DI) water was used to dissolve graphene powder. After processing the graphene suspension (2 mg/mL) for 3 hours (3 s on, 3 s off) in an ultrasonic crusher, the powdered graphene was vacuum-dried to a nano size. In an ice bath, a solution of graphene and $KMnO_4$ (1:6 wt) was mixed with a combination of H_2SO_4 and H_3PO_4 at a volume ratio of 1:8. The mixture was then heated to 60°C and stirred continuously for 15 hours. After the final product had reached room temperature, it was added to ice water that contained H_2O_2. Following that, 100 mL of water, 100 mL of 30% HCl, and 100 mL of ethanol were used twice to wash the remaining solid material. Following the completion of the repeated washing procedure, the remaining material was coagulated using 100 mL of ether and filtered through a 0.32 μm pore size membrane. To obtain graphene oxide powder, the solid on the filter was collected using deionized water and freeze-dried under a vacuum.

Next, carboxylated graphene oxide (NGO) was prepared. The process of preparing carboxylic acid-functionalized graphene oxide involves a strongly alkaline reaction with chloroacetic acid to convert some of the oxygen-containing groups of the graphene oxide to carboxyl groups. In simple terms, 2.4 g of chloroacetic acid and 2 g of NaOH were added to 200 mL of graphene oxide solution (1 mg/mL). At room temperature, the mixture was sonicated for four hours. After neutralizing the resultant solution with HCl to a pH of 7, it was refined by repeatedly rinsing and filtering. Finally, the resultant product redispersion and underwent lyophilization.

Preparation of NGO-SB-204990-DOX

According to previous studies,[25,33] SB-204990 (1 mg/mL) and NGO (2 mg/mL) solution were mixed, and DI water was adjusted to 3 mL. The reaction mixture was swirled at room temperature for the entire day. The NGO-SB-204990 (NS) precipitate was obtained by centrifugation (10,000 × g for 20 min). The precipitate was washed three times with DI water to remove unbound SB-204990. Subsequently, the NS precipitate was redissolved in DI water, and DOX (1 mg/mL) was added. The mixture was then stirred overnight at room temperature. The precipitate was collected and centrifuged (10,000 × g for 25 min). It was then cleaned three times with DI water to remove unbound DOX. The NGO-SB-204990-DOX nanomaterials were obtained by removing large NGO particles using a needle filter (0.3 μm) and freeze-drying.

Characterization of NGO

The structures of NGO, NS, and NSD were determined by infrared spectroscopy (Thermo Fisher Scientific) and UV-Vis absorption spectroscopy (Nicolet Is50, Thermo Fisher Scientific). The morphology of the drug-carrying particles was examined using transmission electron microscopy (TEM; JEOL JEM-2000 EXII, Japan). The surface morphologies of the nanoparticles were examined using scanning electron microscopy (SEM, JEOL 7900F, Japan). After the samples were mixed with DI water, a zeta potential analyzer (Zetasizer Nano ZS 90, UK) was used to assess the potential and size of the nanoparticles.

In vitro Stability

Prepare 1 mL each of PBS solution and FBS solution of NGO, NS and NSD (all at a concentration of 1 mg/mL for NGO), place in a 1.5 mL centrifuge tube and let stand at room temperature. The stability of the solutions in the centrifuge tubes was observed and recorded at different time intervals.

Loading and Release of SB-204990 and DOX

For SB-204990 loading, 0.1 mg of NGO and various weights of SB-204990 were combined in 1 mL of solvent (PBS, pH 7.4) and stirred at room temperature for one day. Centrifugation (10,000 × g, 20 min) was performed, and the precipitate was collected. Subsequently, the precipitate was vacuum-dried, weighed, and utilized for DOX loading. For DOX loading, the product from the previous step was mixed with different masses of DOX in a solvent (PBS, pH 7.4), stirred overnight at room temperature, centrifuged (10,000 g, 25 min), and the precipitate was collected. To calculate the unbound SB-204990 and DOX, the supernatants obtained from the two centrifugations were separated, and a UV-Vis spectrophotometer was used to measure the quantities of unbound SB-204990 and DOX at absorption wavelengths of 200 and 480 nm, respectively. The loading efficiency (LE) and loading content (LC) were calculated using Equations (1) and (2):

$$\text{Loading efficiency } (\%) = \frac{\text{mass of drug in nanocarrier}}{\text{mass of drug in nanocarrier} + \text{mass of nanocarrier}} \times 100 \tag{1}$$

$$\text{Loading content} = \frac{\text{mass of drug in nanocarrier}}{\text{mass of nanocarrier}} \tag{2}$$

The release of DOX and SB-204990 was determined as follows: Two PBS solutions were prepared with different pH values (7.4 and 5.5). NS and NSD solutions were prepared using PBS as the solvent, with a carrier-to-drug ratio of 1:1 (w/w). The experiment was conducted in a shaker at 37 degrees Celsius for varying durations (1, 2, 4, 8, 12, 24, 48, and 72 hours). Samples were collected by centrifugation at 12,000 rpm for 15 min to determine drug release, and the supernatant was separated at predefined intervals. Subsequently, an equivalent amount of fresh PBS was added to replace the supernatant. The release of SB-204990 and DOX was determined by combining the peak heights at 200 and 480 nm, respectively, using a UV-Vis instrument with standard curves of SB-204990 and DOX. Each drug release test was performed in triplicate, and Equation (3) was used to calculate the average results.

$$\text{Drug release } (\%) = \frac{\text{mass of drug release}}{\text{mass of drug in nanocarrier}} \times 100 \tag{3}$$

In vitro Photothermal Properties

To prepare the solutions, 100 μL of NGO, NS, and NSD solutions at various concentrations (0.1, 0.2, 0.5, 1 mg mL^{-1}) were made in 200 μL EP tubes using DI water as the solvent. Subsequently, an 808 nm NIR laser (Honglan, China) illuminated the EP tubes from the top at different energy levels (1, 1.5, 2, and 2.5 W cm^{-2}). Thermal images were captured at various intervals using a Thermo GEAR G100 EX infrared camera (Nippon Avionics, Japan) positioned beside the tubes. The peak temperature profile was plotted against time, and the photothermal conversion efficiency was then calculated. The photothermal conversion efficiency can be determined using the following formula:

$$\eta = \frac{hS\left(T_{max-}T_{max,water}\right)}{I\left(1-10^{-A808}\right)} \tag{4}$$

$$t = -T_S \ln \theta \tag{5}$$

$$T_S = \frac{mC}{hS} \tag{6}$$

$$\theta = \frac{T - T_{sur}}{T_{max} - T_{sur}} \tag{7}$$

Where η represents the photothermal conversion efficiency, m denotes the solution mass, and C denotes the heat capacity. The heat transfer coefficient (h) and surface area (S) of the vessel are also provided. The power density of the 808 nm laser is denoted by I, where A808 is the absorbance of the NSD at 808 nm, and T_{max} and $T_{max,\ water}$ represent the highest temperatures of the NSD and water, respectively, at the time of irradiation. The time constant is denoted by T_S.

In vitro Blood Compatibility Assay

To evaluate the hemocompatibility of the NSD, blood was collected from mice by centrifugation at 3000 × g for 15 min, and the supernatant was discarded. Twenty microliters of erythrocytes were incubated in various concentrations (25, 50, 100, 200, and 400 μg/mL) of NSD nanoparticles for 1 h at 37 °C, with DI water as the positive control and PBS as the negative control. The hemolysis rate was determined using Formula (8) after centrifugation by measuring the absorbance of the supernatant at 542 nm.

$$\text{Hemolysis } (\%) = \frac{OD_{542}\text{of NSD} - OD_{542}\text{of PBS}}{OD_{542}\text{of water} - OD_{542}\text{of PBS}} \times 100 \quad (8)$$

In vitro Cytotoxicity

Cell viability was estimated using a CCK-8 kit assay. Briefly, 96-well plates were seeded with cells (6000 cells/well) in triplicate and allowed to grow overnight. Subsequently, the cells were treated with the drug for various periods. Absorbance was measured at 450 nm using a Varioskan Flash enzyme marker (Thermo Fisher Scientific). The half maximum inhibitory concentration (IC_{50}) from the dose-response curve was utilized to determine drug sensitivity. The ratio of live to dead cells was determined using a Calcein AM-PI staining kit. Cells (5×10^4/well) were seeded into 24-well plates and cultured to confluence. Following treatment with the drugs for 24 hours, Calcein AM was incubated in the dark for 10 minutes, and PI was then incubated for 5 minutes, also in the dark, before being washed three times with PBS. Images were captured using an inverted fluorescence microscope. To ascertain whether apoptosis contributed to cell death, a V-FITC/PI apoptosis detection kit was employed. After an 8-hour drug treatment with the designated doses, cells were stained for 15 minutes at room temperature in the dark using 5 μL of membrane-associated protein V-FITC and 5 μL of PI. Subsequently, a flow cytometer (FACSCalibur, BD Biosciences, USA) recorded at least 10,000 events, and the data were analyzed using NovoExpress software.

Cell Uptake

The cellular uptake of free DOX and DOX-loaded nanocarriers by SCC-15 cells was examined qualitatively and quantitatively using flow cytometry and laser confocal fluorescence microscopy. Cells were cultured for 24 hours in 6-well plates (6×10^5/well). Subsequently, cells were treated with both DOX (ND and NSD)-loaded nanocarriers (DOX at a uniform concentration of 10 ug/mL) and free DOX (as a positive control). The Free Dox+Laser and NSD +Laser groups had a 5-minute exposure to an 808 nm NIR laser. Untreated cells were used as negative controls. After 4 hours, the cells were collected and evaluated by FACSCalibur flow cytometry to determine the intensity of the fluorescent signals taken up by DOX. Additional confirmation of the fluorescence intensity of DOX and DOX-loaded nanocarrier uptake by the cells was performed using a TCS SP5 laser confocal fluorescence microscope (Leica, Germany). Cells were inoculated into 24-well plates (with crawler sheets placed in the well plates) and grown for 24 hours. The following day, DOX and DOX-loaded nanocarriers were co-incubated with the cells for four hours. After three washes with PBS, the cells were immobilized on crawler sheets using paraformaldehyde. The cytoskeletons and nuclei were analyzed using FITC-labeled ghost pen cyclic peptides (Solarbio, China) and DAPI (Solarbio, China), respectively. Laser confocal fluorescence microscopy was used to measure the fluorescence intensity of intracellular DOX.

Quantification of Acetyl-CoA, Free Fatty Acid, and Cholesterol

Acetyl-CoA, free fatty acid, and total cholesterol levels were quantified in SCC-15 cells and tumor tissues using specific assay kits. SCC-15 cells were seeded into 6-well plates (6×10^5/well) and cultured for 24 hours. Subsequently, SCC-15 cells were co-incubated with SB-204990 and NS for predetermined durations (24 h, 48 h, 72 h), while untreated cells served as controls. Cells were prepared by subjecting them to a 5-minute, 1000-g centrifugation. The cells were then lysed by repeated freeze-thaw cycles or sonication, followed by a 10-minute, 1500-g centrifugation at 4 °C. The resulting supernatant was utilized to measure the levels of acetyl-coenzyme A, free fatty acids, and total cholesterol in SCC-15 cells, following the instructions provided by the reagent vendor. For tumor tissues, mechanical homogenization was

carried out by adding PBS at a ratio of weight (g) to volume (mL) = 1:9. After centrifugation at 2400 × g for 10 minutes, the supernatant was collected to determine the levels of acetyl-coenzyme A, free fatty acids, and total cholesterol in tumor tissues, following the instructions provided by the reagent vendor.

In vivo Anti-Tumor Efficiency

The Laboratory Animal Ethics Committee of Shanxi Medical University approved all procedures under Ethics No. KQDW-2024-003. All animal experimental procedures experimentally complied with the Guidelines for the Breeding and Use of Laboratory Animals and the Animal Welfare Law in China. Five-week-old male thymus-free BALB/c nude mice (18–20 g) were utilized for the experiments. The right hind limbs of the mice were subcutaneously injected with 100 μL of sterile saline containing 5×10^6 SCC-15 cells. Upon the tumors reaching approximately 80–100 mm^3 in size, mice were randomly allocated into ten groups (n = 3). Nude mice were intratumorally injected with PBS, SB-204990, Free DOX, SB-204990+Free DOX, NS, NSD, NGO+Laser, SB-204990+Free DOX+Laser, NS+Laser, or NSD+Laser at a dose of 5 mg kg^{-1} (DOX). Those injected with NGO, SB-204990+Free DOX, NS, or NSD were immediately subjected to 808 nm laser irradiation (1.5 W cm^{-2}, 5 min) at the tumor site. An infrared camera recorded temperature and images of the treatment site at designated times. Throughout the treatment, tumor sizes and body weights of the ten groups of nude mice were measured. Tumor volume was calculated using the formula: length (mm) × width (mm) × width (mm) × 0.5. At the end of treatment, the major organs and tumors of nude mice were collected, and the tumor inhibition rate of each group was calculated. The formula was calculated as (average volume of tumor in PBS group - average volume of tumor in the treatment group) / average volume of tumor in PBS group * 100%. A portion of the xenograft tumor tissue specimen was fixed with 4% paraformaldehyde, embedded in paraffin, sectioned, and stained with H&E eosin. Another part (PBS, SB-204990, NS) was homogenized for tissue analysis to detect levels of acetyl coenzyme A, free fatty acids, and total cholesterol. Euthanasia was performed using an overdose of intraperitoneal anesthesia, with animal heartbeats checked post-injection to confirm the cessation of vital signs.

Statistical Analysis

Standard deviation (SD) was used to express the data. One-way analysis of variance (ANOVA) or two-tailed Student's t-tests with 95%, 99%, and 99.9% confidence intervals were used to determine statistical significance. The significance thresholds were set at *P < 0.05, **P < 0.01, ***P < 0.001, and ****P<0.0001.

Results

ACLY Expression is Upregulated in OSCC

To determine whether ACLY was highly expressed in OSCC, we conducted IHC analysis on tumors and normal tissues from OSCC patients. Immunohistochemistry revealed (Figure 1A) that ACLY was expressed in both the nucleus and cytoplasm of OSCC cells, whereas it was only weakly expressed in the cytoplasm of normal tissues and significantly lower than in cancerous tissues (P<0.01). This finding aligns with previous studies by Chen et al and Toshiro et al on breast and non-small-cell lung cancers.[34,35] We evaluated the mRNA levels of ACLY in human tongue squamous carcinoma cell lines such as SCC-15, SCC-25, and CAL-27, and HOK (human normal oral keratinocytes), as well as the protein levels of ACLY in SCC-15 and HOK cells. Our results showed that ACLY mRNA (Figure 1C) and protein (Figure 1B) expression were much higher in OSCC cells compared to HOK cells. Together, these findings suggest that ACLY expression is upregulated in OSCC cells. Utilizing the ACLY-specific inhibitor SB-204990, we co-incubated SCC-15 and HOK cells. CCK8 experiments revealed (1D) that the inhibition of cell proliferation by SB-204990 increased in a dose- and time-dependent manner. Following a 24-hour co-incubation period with cells at a concentration of 160 μg/mL of SB-204990, the viability of SCC-15 and HOK cells dropped to 27% and 59%, respectively. Particularly noteworthy, SCC-15 cells exhibited more pronounced reproductive suppression at the same dose and time, attributed to their more vigorous lipid metabolism[36] and higher ACLY expression in cancer cells. This suggests the potential use of appropriate concentrations of ACLY inhibitors to treat cancer without harming normal cells. In addition, the results of transwell migration (Figure 1F) and wound healing assays (Figure 1G) showed that the migration ability of SCC-15 cells was

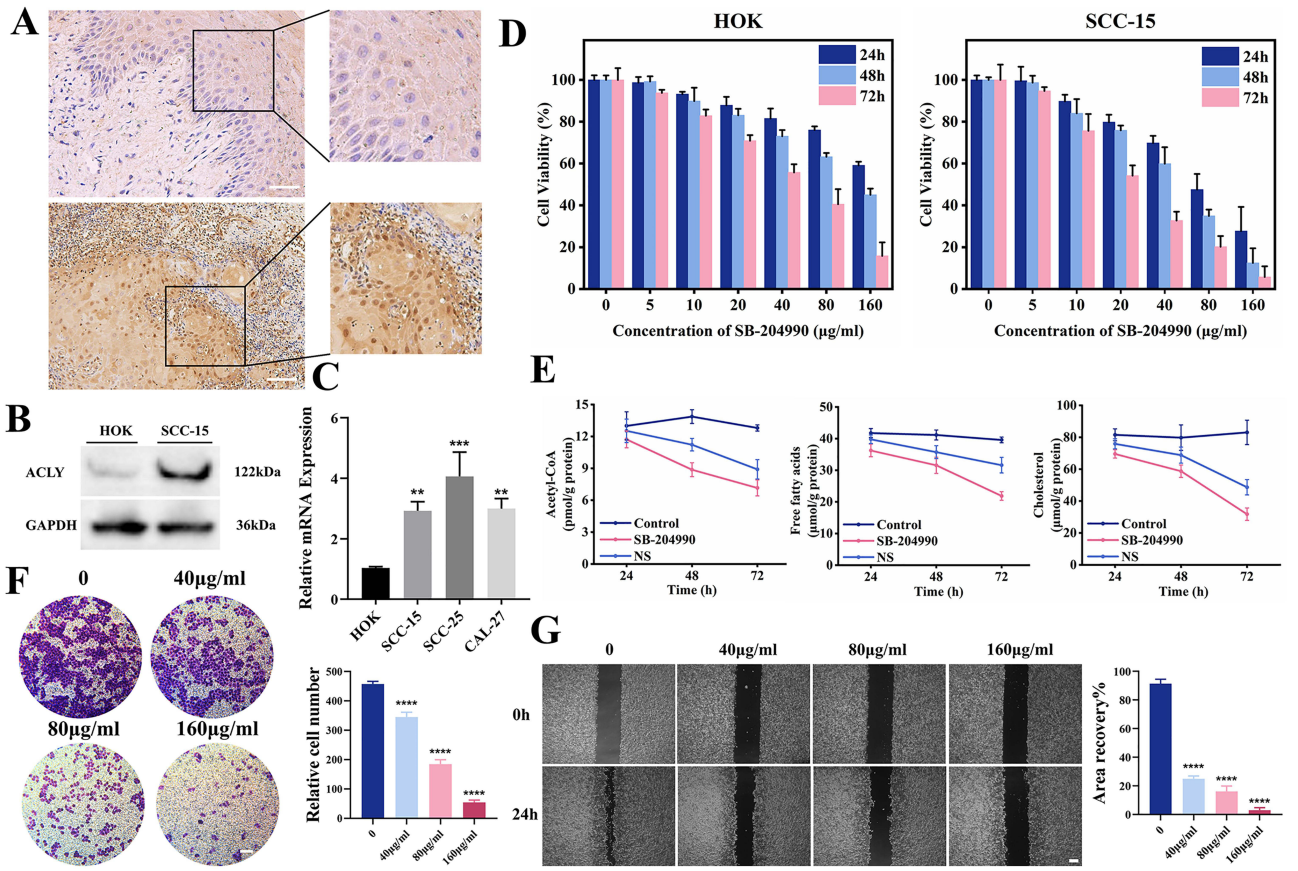

Figure 1 (**A**) Immunohistochemical images of ACLY staining in normal and OSCC tissues. Scale bar: 100 μm. (**B**) Differential protein expression of ACLY in HOK and SCC-15 cells. (**C**) Differential mRNA expression of ACLY in HOK, SCC-15, SCC-25, and CAL-27 cells. (mean ± S.D. n = 3. **P<0.01, ***P<0.001. *Indicates comparisons with the group with HOK.) (**D**) Viability of HOK and SCC-15 cells after incubation with SB-204990. (mean ± S.D. n = 5.) (**E**) Untreated, treated with SB-204990, NS for 24 h, 48 h, and 72 h levels of acetyl coenzyme A, free fatty acids, and cholesterol within SCC-15. (mean ± S.D. n = 5.) (**F**) Transwell chamber migration experiment of SCC-15 cells after incubation with SB-204990. Scale bar: 100 μm. (mean ± S.D. n = 3. ****P<0.0001. *Indicates comparisons with the group with a concentration of 0.) (**G**)Wound healing experiment of SCC-15 cells after incubation with SB-204990. Scale bar: 200 μm. (mean ± S.D. n = 3. ****P<0.0001. *Indicates comparisons with the group with a concentration of 0.).

reduced after co-culture with SB-204990, and the higher the dose, the more obvious the reduction. In conclusion, the results suggest that ACLY can be used as an anticancer target and SB-204990 is a well-performing anticancer drug. To investigate the effect of ACLY inhibition on lipid levels, we assessed the concentrations of several key factors involved in lipid metabolism post-ACLY inhibition. As depicted (Figure 1E), levels of acetyl coenzyme A, free fatty acids, and cholesterol decreased in SB-204990-treated SCC-15 cells compared to untreated SCC-15 cells, with this decrease becoming more pronounced over time. The decrease in the NS-treated group was even smaller, likely due to the incomplete release of SB-204990 from the NGO. Our study lends support to the hypothesis of many researchers regarding the alterations in lipid metabolism following ACLY inhibition in cancer cells.[37,38] Once the lipid metabolic pathway is disrupted, intracellular concentrations of fatty acids and cholesterol will decrease with decreasing concentrations of acetyl coenzyme A. Acetyl coenzyme A serves as a precursor for the synthesis of many important lipids and is essential for histone acetylation.[39,40] Consequently, cancer cells face a shortage of vital nutrients, leading to cell death. In addition, the harsh survival environment may increase the sensitivity of tumor cells to chemotherapeutic drugs, resulting in a synergistic "1+1>2" effect of killing tumor cells. Therefore, we surmised that inhibition of ACLY not only exerts an anticancer effect but may also improve chemotherapy resistance in OSCC due to the reduction of lipid levels, resulting in a better synergistic antitumor effect.

Preparation and Characterization of NSD

The graphical abstract illustrates the flowchart of the NSD preparation process. We synthesized NSD nanoparticles by sequentially linking SB-204990 and DOX through hydrogen bonding and π-π stacking. As shown in Figure S1, the

toxicity of NGO's becomes greater with increasing concentration. After being treated with 200 μg/mL of NGO for 24 hours, the survival rates of HOK and SCC-15 cells maintained approximately 90%. At 400 μg/mL, the concentration of NGO caused a drop in HOK and SCC-15 cell survival rates to 72% and 75%, respectively. We decided to use 200 μg/mL as the final concentration for biosafety concerns. In addition, in the next tests, the semi-inhibitory concentration for SB-2049909 (73.65 μg/mL) and DOX (4.489 μg/mL) incubating with SSC-15 cells for a full day (Figure S2) was employed.

The morphologies of NGO, NS, and NSD are depicted in Figure 2A. Compared to pristine NGO, the laminar structure of NS thickens and particles appear on the surface. NSD displays an increased presence of particles on the lamellar structure, indicating successful loading of SB-204990 and DOX. Surface micromorphologies of NGO, NS, and NSD are shown in Figure 2B. NGO exhibits a laminar wrinkle-like structure, while NS and NSD surfaces become smoother with noticeable particles post-SB-204990 and DOX loading, possibly due to their adsorption altering the original morphology of NGO. UV-vis analysis in Figure 2C reveals the absorption peak at 230 nm, typical of C=O, in NGO spectra. The characteristic absorption peaks of NSD at 200 nm and 480 nm provided direct evidence of SB-204990 and DOX adhesion. FTIR spectra (Figure 2D) show broad absorption peaks around 3400 cm^{-1}, representing -OH stretching vibration in NGO, NS, and NSD. A shift in the C=O vibrational band from 1640 cm^{-1} in NGO to 1655 cm^{-1} in NS and NSD is observed. NS exhibits a stretching vibration of -Cl at 1281 cm^{-1}, while NSD presents an absorption peak at 682 cm^{-1}, attributed to -NH- bonding, indicating successful loading of SB204990 and DOX onto NGO. Figure 2E displays the average hydrodynamic diameters of NS and NSD, which show only a slight increase compared to NGO, with all particles remaining under 300 nm. In addition, the size distributions of NGO, NS and NSD nanoparticles were modeled as single peaks with PDI values of 0.23 ± 0.02, 0.21 ± 0.02, and 0.24 ± 0.01, respectively. Zeta potential distributions (Figure 2F) indicate a shift in NS potential to a more negative value (−19.6 mV) compared to NGO (−17.7

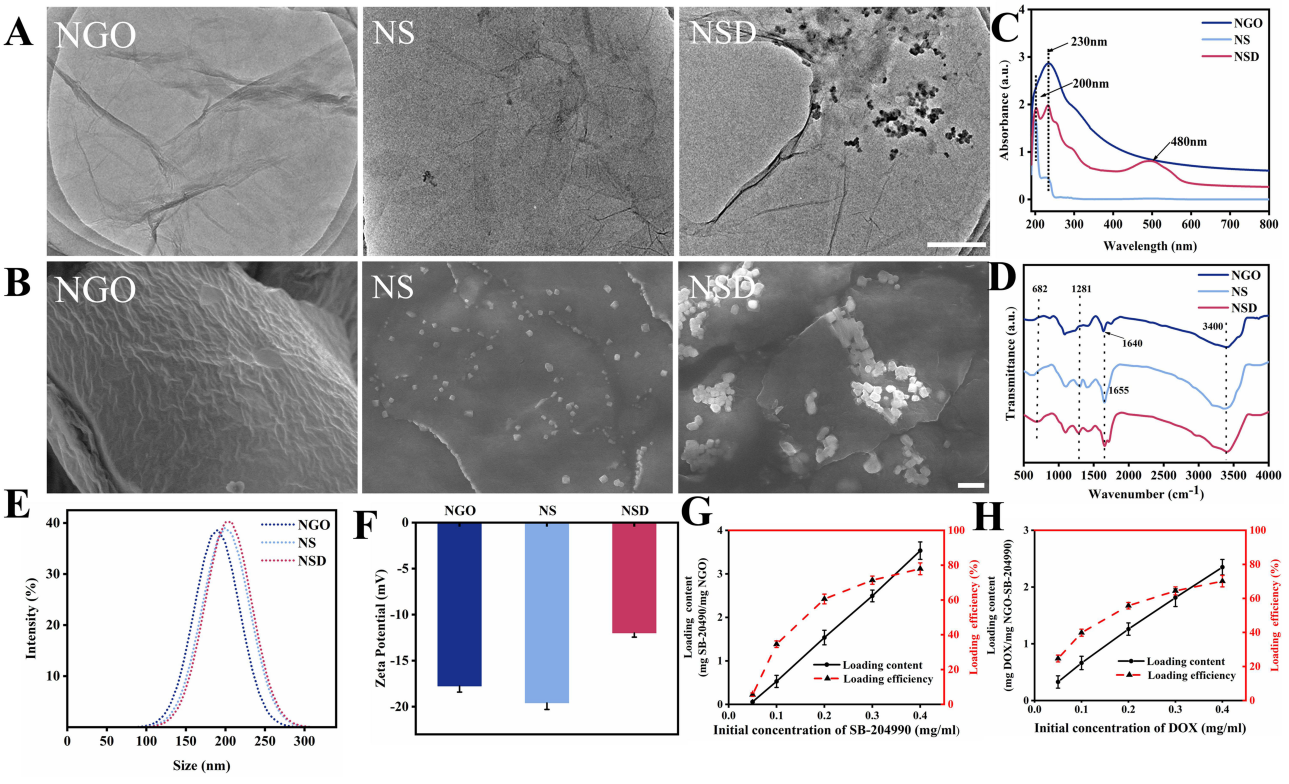

Figure 2 (**A**) TEM images of NGO, NS, NSD. Scale bar: 0.5 μm. (**B**) SEM images of NGO, NS, NSD. Scale bar: 1 μm. (**C**) UV-vis spectra of NGO, NS, NSD. (**D**) FT-IR spectra of NGO, NS, NSD. (**E**) Particle size distribution curves of NGO, NS, NSD. (**F**) Zeta potential distribution of NGO, NS, NSD. (**G**) Loading efficiency and loading content of SB-204990 on NGO (0.1mg). (**H**) Loading efficiency and loading content of DOX on NGO-SB-204990 (0.1mg).

mV), while NSD shows a potential rise to −12 mV, consistent with the expected potential change post-SB-204990 and DOX loading. All the above studies have shown that NSD nanoplatforms have been successfully prepared.

In vitro Stability of NSD

To further evaluate the stability of the nanocarrier systems, we dissolved different nanosystems in PBS and FBS. As shown in Figure S3, NGO, NS and NSD were stably dispersed in both PBS and FBS for more than 6 days. The results show that the loading of SB-204990 and DOX does not significantly reduce the stability of NGO. This excellent physiological stability facilitated the intact delivery of loaded anticancer drugs from NGO to the site of action and ensured the biocompatibility of NSD.

NSD Loading and Simulated Release in vitro

Next, we evaluated the drug-carrying capacity and release behavior of NSD. For SB-204990 loading, we mixed NGO (0.1 mg) with SB-204990 (0.05 to 0.4 mg) in 1 mL of PBS to assess the loading content (LC) and loading efficiency (LE) of the drugs. As the concentration of SB-204990 increased, the LC increased from 0.05 to 3.53 mg/mg. The LE increased from 6% to 78% (Figure 2G). Under the same conditions, the LC of DOX increased from 0.32 to 2.35 mg/mg, and the LE increased from 25% to 70% (Figure 2H). With an increase in drug concentration, both SB-204990 and DOX showed significant increases in loading content and efficiency, demonstrating the powerful loading capacity of NGO. The release of SB-204990 and DOX is shown in Figure 3G and H, respectively. We performed in vitro release experiments at 37°C for 72 h in PBS at different pH values (7.4, 5.5). The release trends of loaded SB-204990 and DOX under PBS treatment at different pH values flattened over time. At pH 7.4, the release of SB-204990 and DOX at 72 h was 51.2% and 57.8%, while in 5.5 PBS, the release of SB-204990 and DOX reached 72.1% and 77%, respectively. The release in an acidic environment was noticeably higher than that in a neutral environment, demonstrating the pH responsiveness of NSD. The release of NSD was accelerated in the acidic environment of the tumor after drug loading. This may be because hydrogen bonds are more easily hydrolyzed and broken under acidic conditions, making them unstable.[25] The tumor microenvironment is acidic, whereas the physiological pH is close to neutral; therefore, SB-204990 and DOX on NSD can remain relatively stable in normal tissues and physiological environments, whereas they can be released in the tumor microenvironment.[41] This difference in release can minimize the loss of drugs outside cancer cells, thereby increasing the intracellular drug concentration, exerting higher cytotoxicity, and lessening the harmful effects of anticancer medications on the body.[42] In addition, this slow-release property of NSD helps to prolong the duration of drug action and increase the anticancer effect compared to the direct action of free drugs. We added 808 nm laser irradiation at two pH levels (7.4, 5.5) to examine the influence of photothermal irradiation on drug release. The cumulative release rates of laser-irradiated NSD for SB-204990 and DOX were 79.1% and 83.3%, respectively. The results indicated that photothermal could promote the release of SB-204990 and DOX on NSD, and photothermal had good combined anticancer effects with chemotherapy and starvation therapy.

In vitro Photothermal Performance Analysis of NSD

We conducted a series of photothermal experiments using phosphate-buffered saline (PBS) as a control group and irradiated a specified concentration of NSD with an 808 nm laser (1.5 W cm^{-2}) for 5 minutes to explore the photothermal capabilities of NSD. As shown in Figure 3A, the temperature of the NSD-treated group reached 63°C with a temperature change of 33.9 °C, which was not significantly different from the NGO and NS treatment groups. This final temperature is sufficient to destroy cancer cells.[43] Moreover, this finding suggests that the photothermal conversion capability of NSD is not diminished by the adsorption of DOX and SB-204990.

In contrast, the temperature of the PBS group reached 33.2 °C with a slight temperature change of 6.7 °C. These results demonstrate that NSD exhibits good photothermal performance. We also observed concentration- and irradiation power-dependent changes in temperature, which increased with higher concentrations of the NSD solution and irradiation power (Figure 3B and C). Irradiation of solutions with different concentrations (0.1, 0.2, 0.5, and 1 mg mL^{-1}) using an 808 nm laser (1.5 W cm^{-2}) for 5 minutes resulted in final temperatures of 42.7 °C, 63 °C, 66.4 °C, and 73.4 °C, with temperature increases of 15.9 °C, 33.9 °C, 38 °C, and 46.7 °C, respectively. Similarly, for different irradiation powers (1,

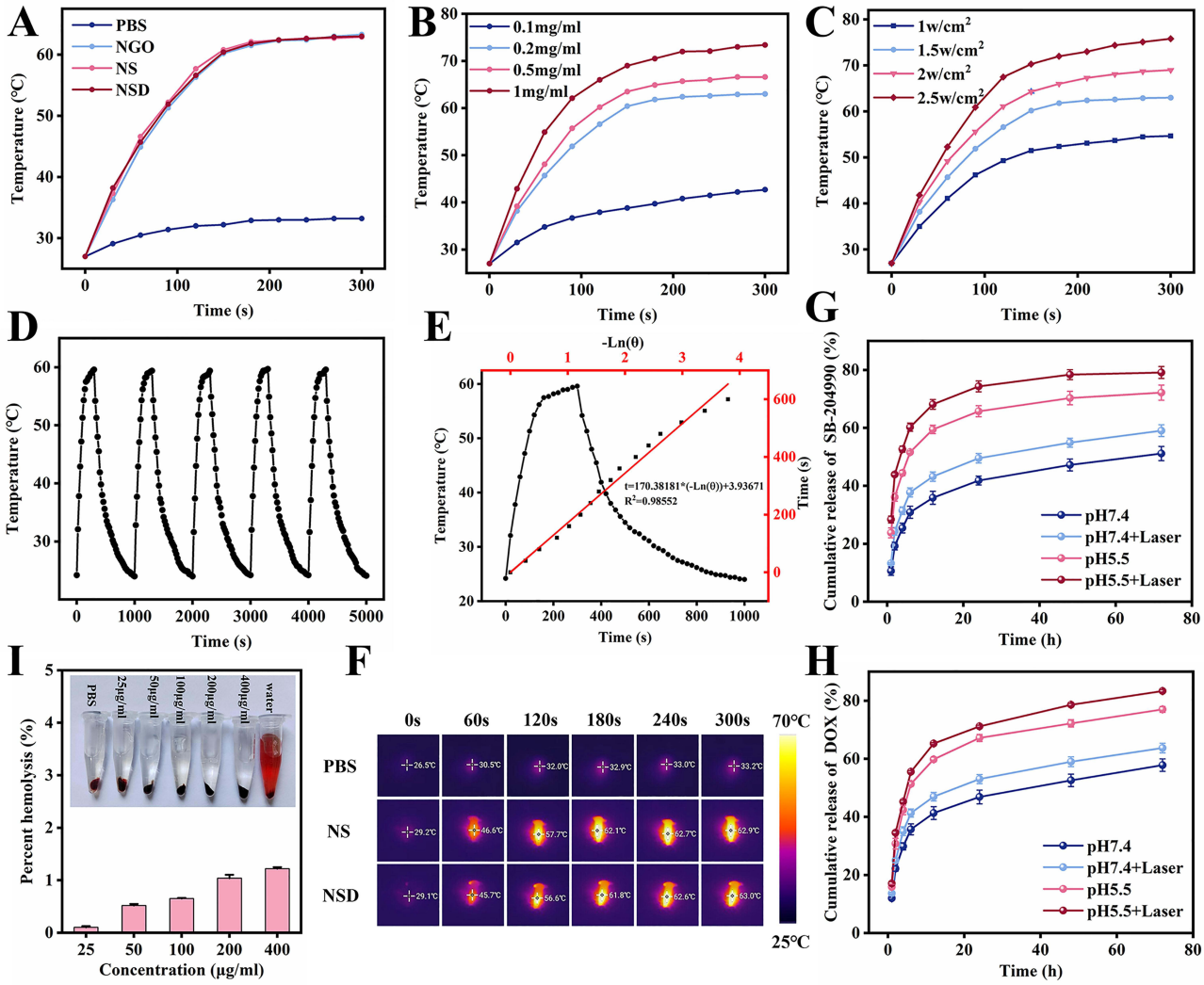

Figure 3 (**A**) Photothermal heating curves of PBS, NGO, NS, NSD. (1.5 W/cm^2, 0.2 mg/mL) (**B**) Photothermal heating curves of NSD at different concentrations. (**C**) Photothermal heating curves of NSD at different powers. (**D**) Photothermal temperature curves of NSD over five laser cycles. (**E**) Linear analysis of the photothermal performance of NSD under room temperature cooling. (**F**) Thermal imager images of PBS, NS, and NSD at 1.5 W/cm^2, 0.2 mg/mL. (**G**) Drug release profiles of SB-204990 at different pH. (**H**) Drug release profiles of DOX at different pH. (**I**) Hemolysis rate of different concentrations of NSD.

1.5, 2, and 2.5 W cm^{-2}), the temperature changes were 26.3 °C, 33.9 °C, 40.7 °C, and 48 °C, and the final temperatures reached 54.7 °C, 63 °C, 69 °C, and 75.8 °C, respectively. Based on considerations of the anticancer effect and protection of normal tissues, we chose 1.5 W cm^{-2} of the 808 nm laser for subsequent experiments. Evaluating the photothermal stability of NSD is crucial for further clinical applications (Figure 3D). Under 808 nm laser irradiation, no significant decay in the maximum temperature of the solution was observed during five laser on/off cycles. This suggests that NSD exhibits excellent stability for future clinical applications. We also examined the photothermal conversion ability of NSD (Figure 3E) and found that the photothermal conversion efficiency of NSD was 26.2% after systematic calculation. The real-time infrared thermography signals in Figure 3F demonstrate temperature changes in the PBS, NS, and NSD groups. The results of the photothermal performance experiments indicate that NSD is a promising photothermal therapy (PTT) nanocomposite.

Hemolysis Experiments

The potential for hemolysis resulting from the nonspecific interaction of nanoparticles with hemoglobin could significantly affect the practical use of nanomaterials in the medical field.[44] To assess hemocompatibility, we conducted

hemolysis experiments on the NSD (Figure 3I). PBS served as the negative control, while DI water served as the positive control. Our findings indicate that hemolysis occurred in the positive control group but not in the negative control group. The hemolysis rate of NSD within the concentration range of 25–400 μg mL^{-1} increased with concentration. However, even at concentrations up to 400 μg mL^{-1}, the hemolysis rate remained low at just 1.22%, significantly below the threshold of 5%.[45] Therefore, NSD demonstrates good blood compatibility and can be considered safe nanomaterials for medical applications.

Intracellular Uptake of NSD

The ability of nanoparticles to be effectively taken up by tumor cells is crucial for anticancer therapy. We investigated the intracellular uptake of NSD using confocal microscopy (Figure 4A). The results indicated that Free DOX was predominantly localized in the nucleus due to its high affinity for DNA.[46] Moreover, in terms of fluorescence intensity, cells treated with Free DOX exhibited higher intracellular uptake compared to those treated with ND and NSD (Figure 4B). When compared to the Free DOX group, both the average cellular fluorescence intensity and the percentage of cells treated with ND and NSD were significantly reduced. This phenomenon arises because free DOX rapidly enters cells via passive diffusion, while DOX-loaded nanocarriers are absorbed through a slower endocytic pathway. DOX can only access the cell nucleus after being released from the nanoparticles.[41] After irradiation with a laser at a wavelength of 808 nm and a power of 1.5 W/cm^2 for 5 minutes, the fluorescence intensity of DOX in the NSD+Laser group was greatly enhanced, even exceeding that of the Free DOX group, whereas there was no significant change in the fluorescence intensity of the Free DOX+Laser group compared with that of the Free DOX group. This enhancement occurred because the local high temperature not only affected the permeability and fluidity of the cell membrane, thereby increasing endocytosis but also accelerated molecular thermal movement, facilitating drug release.[47] Additionally, there is evidence suggesting that photothermal treatment significantly reduces drug efflux, and the maintenance of high intracellular DOX concentrations through photothermal therapy may underlie its mechanism for ameliorating chemotherapy resistance.

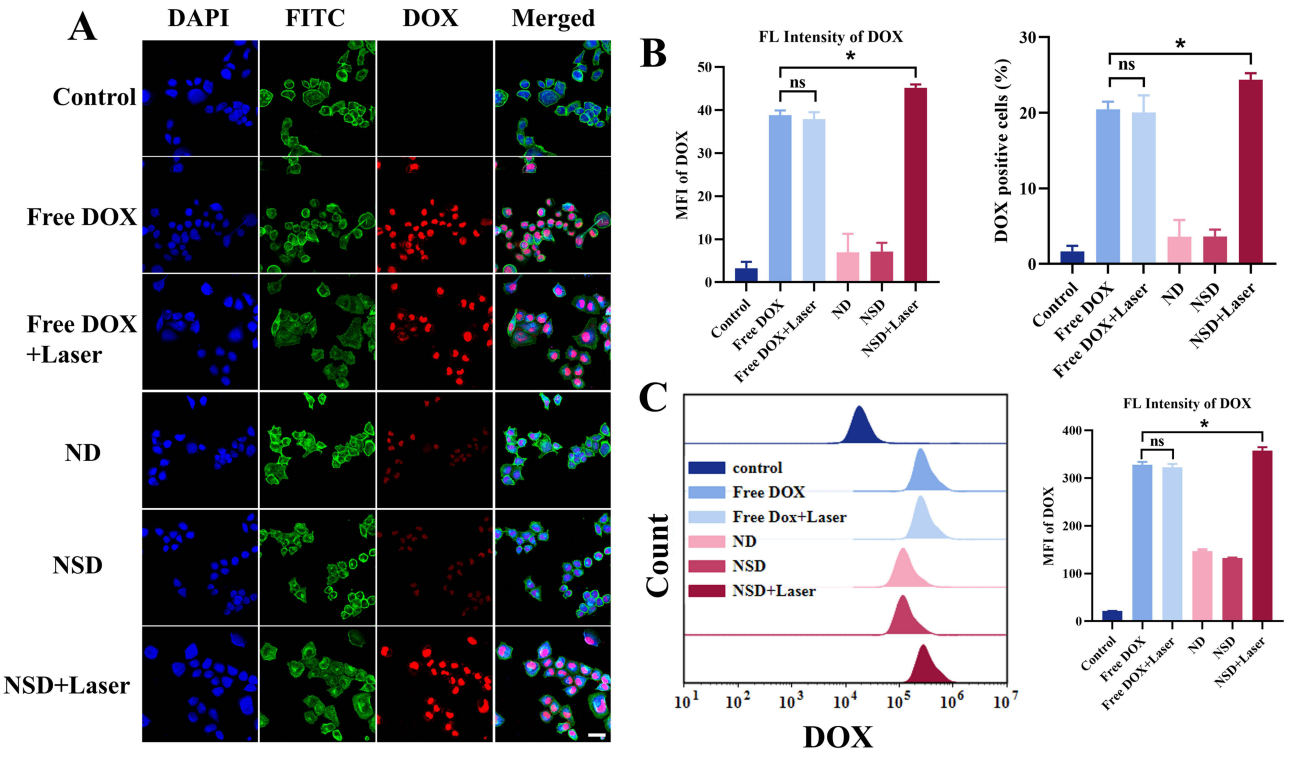

Figure 4 (**A**) Confocal microscopy images of SCC-15 cells after co-incubation with Free DOX, Free DOX+Laser, ND, NSD, NSD+Laser for 4 h. Scale bar: 50 μm. (**B**) Confocal microscopy images of average fluorescence intensity and percentage of positive cells in Free DOX, Free DOX+Laser, ND, NSD, and NSD+Laser groups. (mean ± S. D. n = 3. *P<0.05.) (**C**) Average fluorescence intensity was analyzed by flow cytometry. (mean ± S.D. n = 3. *P<0.05.).

Furthermore, the uptake of NSD was quantitatively assessed by monitoring DOX fluorescence in the cells using flow cytometry. The results (Figure 4C) showed that the average fluorescence intensities of the Free DOX, Free DOX+Laser, ND, NSD, and NSD+Laser groups were 328, 322, 147, 132, and 357, respectively, consistent with the findings from confocal microscopy (Figure 4A). It can be seen that photothermal therapy enhanced the uptake of NSD by SCC-15 cells as well as the release of DOX and SB-24900 in the NGO, which effectively increased the intracellular drug concentration and enhanced the anticancer effect while improving the chemotherapy resistance, demonstrating the advantages of multimodal synergistic therapy.

In vitro Cytotoxicity and Apoptosis Assay of NSD

To explore the synergistic antitumor effects of lipid starvation, chemotherapy, and photothermal therapy, we evaluated the in vitro cytotoxicity of NSD using the CCK-8 assay. Our results, depicted in Figure 5A, indicate that the cell viability of both NGO-treated SCC-15 and HOK cells remained above 90%, underscoring the safety profile of NGO as a drug delivery vehicle. Furthermore, treatment with the ACLY inhibitor SB-2044990 resulted in viabilities of 52% and 79% for SCC-15 and HOK cells, respectively. This differential reduction can be attributed to the interruption of the lipid metabolism pathway in both cell types and SCC-15 cells exhibiting upregulated ACLY expression and a greater lipid metabolism demand.[48] Similarly, the viabilities of DOX-treated SCC-15 and HOK cells were 52% and 72%, respectively, suggesting that cancer cells are more susceptible to chemotherapeutic agents than normal cells. Notably, SB-2044990 exhibited less impact on normal cells compared to DOX while producing equivalent anticancer effects, suggesting the potential of lipid metabolism-related enzyme inhibitors as promising anticancer therapeutics. The viability of SCC-15 cells in the NSD group decreased to 35%, while that of HOK cells was 65%, indicating that NSD retains a degree of protective effect on normal tissues while maintaining its efficacy against cancer cells. Subsequently, upon increasing the 808 nm laser irradiation (1.5 W/cm^2) as shown in Figure 5B, a decrease in viability was observed across the NGO, NS, ND, and NSD groups compared to no laser irradiation, highlighting the potential of NGO as a photothermic cytotoxic agent. However, the growth inhibition observed with PTT-based single treatment was weak, resulting in only an 18% inhibition in the NGO+Laser group. Nevertheless, photothermal treatment facilitated the accelerated release of SB-204990 and DOX, thereby increasing the intracellular concentration of effective drugs. When photothermal treatment was combined with lipid starvation and chemotherapy, it successfully reduced the survival rate of cancer cells to approximately 20% (Figure 5C). This evidence demonstrates that synergistic treatment can effectively eliminate more tumor cells compared to starvation therapy, PTT, or chemotherapy alone.

In addition, the live/dead cell viability staining assay (Figure 5D) demonstrated a consistent in vitro toxicity pattern as observed in the CCK-8 assay (Figure 5C). In the NSD+Laser group, nearly all cells exhibited red fluorescence with an absence of green fluorescence, indicative of minimal cell survival. Apoptosis was evaluated via flow cytometry using a Membrane-Associated Protein V-FITC/PI Apoptosis Detection Kit (Figure 5E), where the quadrants Q1, Q2, Q3, and Q4 represent dead, late apoptotic, early apoptotic, and viable cells, respectively. While no significant differences were observed in the apoptosis rates among the SB-204990, DOX, and NS+Laser groups, the NSD+Laser group exhibited a notable increase to 33.2%, representing a 27.5% rise compared to the control group. All of these findings support the NSD delivery system's potent synergistic efficacy and notable anticancer effect.

In vivo Photothermal Performance Analysis of NSD

We assessed NSD's in vitro photothermal performance in the preceding section; in this section, we further assess its in vivo photothermal performance. BALB/c nude mouse tumor model was established for follow-up experiments. The tumors of the mice in the PBS, NS, and NSD treatment groups were injected with PBS, NS, and NSD, respectively. The tumor areas of the mice in the three treatment groups were exposed to an 808 nm laser at 1.5 W cm^{-2} for five minutes, as shown in Figure 6B. An infrared thermography camera recorded real-time signals of the tumors, and the tumor temperatures of the mice in the treatment groups were measured. The findings demonstrated that the tumors in the PBS treatment group exhibited weak real-time infrared thermography signals, with the tumor temperature increasing only slightly to 38.7 °C over five minutes. In contrast, the tumor areas of the NS and NSD treatment groups showed increasing

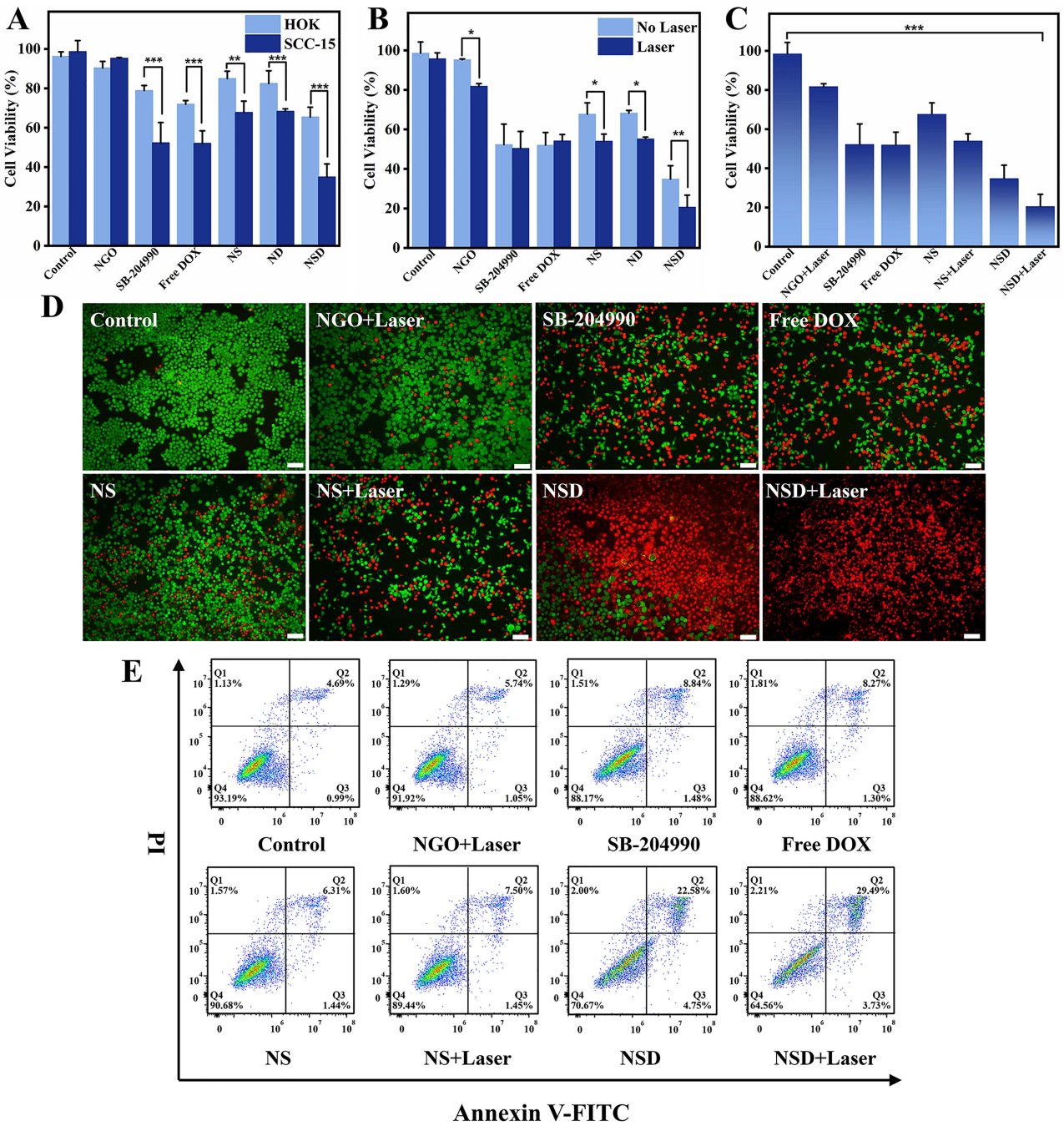

Figure 5 (**A**) Cell viability of HOK and SCC-15 cells after co-incubation with PBS, NGO, SB-204990, DOX, NS, ND, and NSD for 24 h. (mean ± S.D. n = 5. **P<0.01, ***P<0.001.) (**B**) Cell viability of SCC-15 cells after 24 h co-incubation with PBS, NGO, SB-204990, DOX, NS, ND, NSD. "Laser" refers to the exposure of cells to 808 nm laser (1.5 W/cm^2) for 5 min after dosing. (mean ± S.D. n = 5. *P<0.05, **P<0.01.) (**C**) Cell viability of SCC-15 cells after 24 h co-incubation with PBS, NGO+ Laser, SB-204990, DOX, NS, NS+Laser, NSD, NSD+Laser. (mean ± S.D. n = 5. ***P<0.001.) (**D**) Images of differently treated (24 h) SCC-15 cells stained with calcein-AM and PI. Scale bar: 100 μm (**E**) Apoptosis rate of SCC-15 cells with different treatments (8 h) analyzed by flow cytometry.

infrared thermography signals throughout the radiation period, with tumor temperatures reaching 58.3 °C and 58.6 °C, respectively. These results confirm that the photothermal properties of NSD, loaded with SB-204990 and DOX, remained intact and indicate that NSD is a well-performing photothermal material.

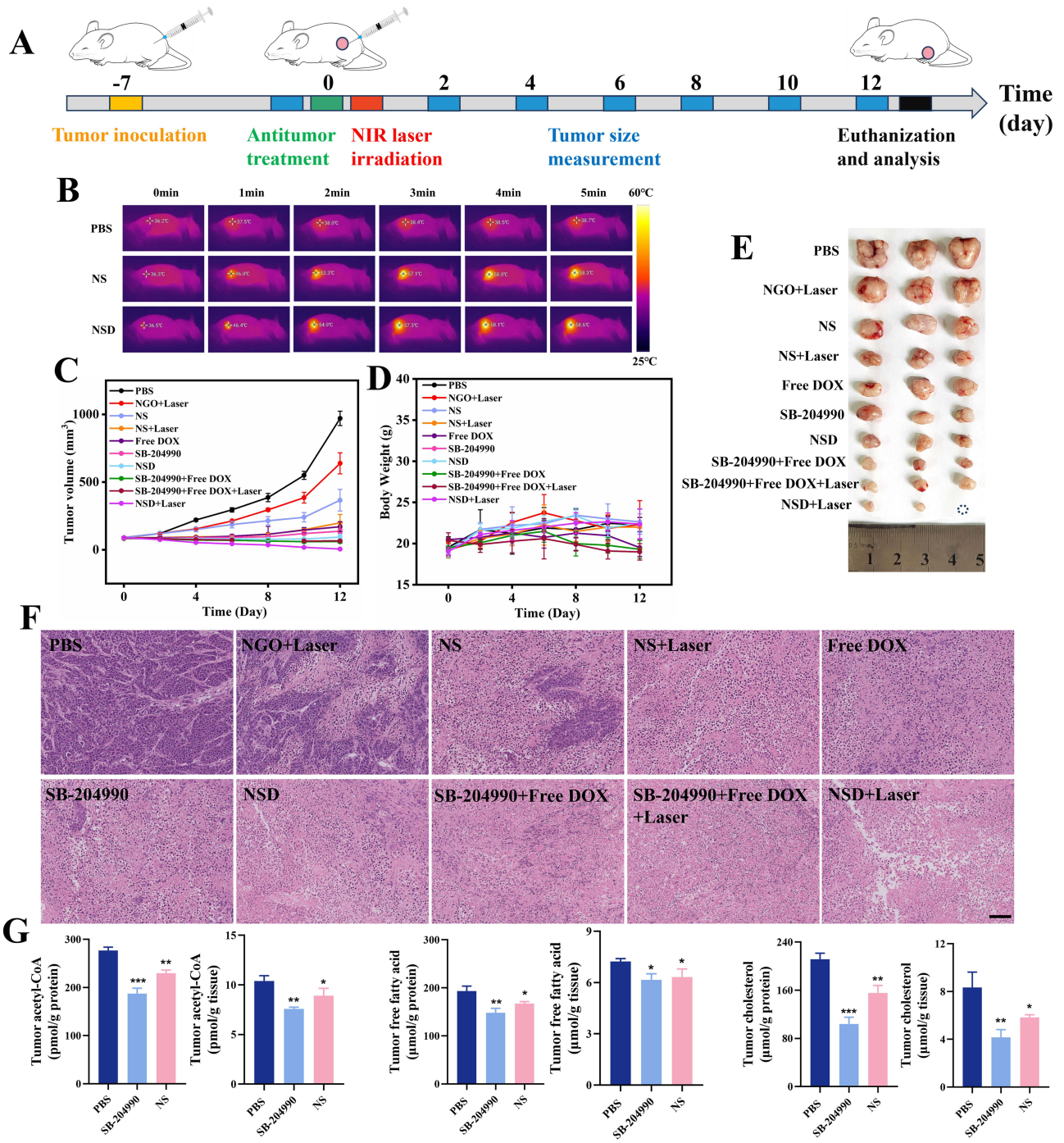

Figure 6 (**A**) Schematic diagram of the anti-tumor process. (**B**) Thermograms of tumor-bearing mice. (**C**) Changes in tumor volume of mice in each group during treatment. (mean ± S.D. n = 3. the statistical analysis of Figure 6C is shown in Figure S4.) (**D**) Changes in body weight of mice in each group during treatment. (mean ± S.D. n = 3.) (**E**) Pictures of tumors excised from mice in different treatment groups after 12 days of treatment. (**F**) Histological analyses of tumor sections by H&E staining after different treatments. Scale bar: 100 μm. (**G**) Determination of acetyl coenzyme A, free fatty acid, and total cholesterol content in tumor tissues, *represents a comparison with the PBS group. (mean ± S.D. n = 3. *P<0.05, **P<0.01, ***P<0.001.).

In vivo Antitumor Effects of NSD

Since NSD exhibited positive anticancer effects in vitro, we further assessed its in vivo anticancer effects in BALB/c nude mice with tumors. The mice were randomly divided into ten groups: PBS, NGO+Laser, NS, NS+Laser, Free DOX, SB-204990, NSD, SB-204990+Free DOX, SB-204990+Free DOX+Laser, and NSD+Laser. The treatment regimens are depicted in Figure 6A. The PBS and NGO+Laser groups showed a rapid increase in tumor volume, as illustrated in

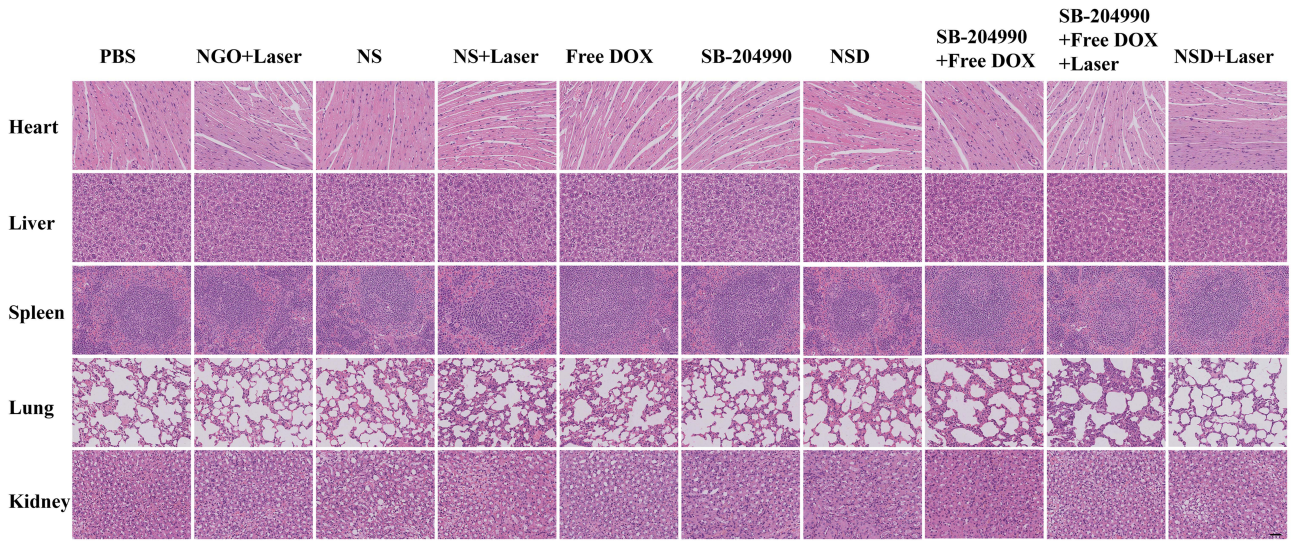

Figure 7 H&E staining of major organs after 12 days of treatment. Scale bar: 50μm.

Figure 6C, while the other groups displayed varying degrees of tumor growth inhibition. Comparing the NGO+Laser, Free DOX, and SB-204990 groups, the NSD+Laser group demonstrated the most promising anti-tumor effect, exhibiting the smallest tumor volume and the highest level of tumor apoptosis (Figure 6F). The combination of lipid starvation therapy, PTT, and chemotherapy showed superior anticancer effects compared to monotherapy. As depicted in Figure 6E, among the tumors resected after 12 days of treatment, the largest tumor was found in the PBS group, the second largest in the NGO+Laser group, and the smallest in the NSD+Laser group, and the tumor in one of the mice completely disappeared, with a tumor inhibition rate of up to 99.4% (Figure 6C). This trend was consistent with the in vitro anticancer effects observed in the respective groups, reinforcing their mutual support. Furthermore, Figure 6D shows that the body weights of mice in the Free DOX group, the SB-204990+Free DOX group, and the SB-204990+Free DOX +Laser group decreased slightly at the later stage, and the body weights of mice in the other subgroups gradually increased over 12 days. Examination of major organ sections from all groups of mice revealed no abnormalities (Figure 7), which ensured the biosafety of the NSD nanoplatform. We noted that the NSD+Laser group showed better therapeutic efficacy (Figure S4) and more biosafety than the SB-204990+Free DOX+Laser group, which demonstrated that the multimodal synergistic therapy of the NSD nanoplatform was superior to the sum of several therapies alone. Additionally, we conducted a lipid analysis correlation of the tumors from the PBS, SB-204990, and NS groups. The results (Figure 6G) showed that the levels of acetyl coenzyme A, free fatty acids, and total cholesterol in the tumors of the SB-204990 and NS groups were reduced to varying degrees compared to those in the PBS group, with statistically significant differences, consistent with the results of the cellular experiments.

Discussion

OSCC is the most frequent malignant tumor of the oral and maxillofacial region.[49] Despite the fact that OSCC is currently treated with surgery, radiation, chemotherapy, or a combination of these approaches, the condition still has a dismal prognosis and a low 5-year survival rate.[50] The majority of advanced patients get combination therapy with numerous chemotherapeutic drugs; nonetheless, their clinical utility is constrained by cytotoxicity and drug resistance.[51]

Lipid metabolism is closely linked to cancer progression and medication resistance, according to recent research.[52] Lipids are vital to cancer cells because they provide them with energy, biofilm components, and signaling chemicals, which are essential to their growth, survival, invasion, and metastasis.[53] In contrast to normal cells, cancer cells experience a number of changes in lipid metabolism, which may have an impact on the development of tumor treatment resistance. Lipid-related mechanisms have been shown to impact therapeutic efficacy through modifications to membrane permeability, regulation of ABC transporter protein activity, impact on mitochondrial function, and drug diffusion.[54]

Cells resistant to chemotherapy exhibit higher cholesterol levels, and higher levels of fatty acid oxidation also promote chemoresistance. Therefore, lipid-lowering therapies become a possibility among the strategies to improve chemoresistance. Furthermore, based on the growth arrest caused by lipid-lowering therapies, lipid metabolism may be a dual-action target for anticancers and for improving tumor cell insensitivity to chemotherapeutic agents.

ACLY is an important enzyme in the first rate-limiting of ab initio lipogenesis and is widely overexpressed in various tumor tissues.[55] ACLY has an upstream advantage over other lipases. For the production of fatty acids, the metabolism of cholesterol, and histone acetylation, ACLY levels and activity are essential.[17] In the present study, we co-cultured SB-204990 and SCC-15 cells and demonstrated that inhibition of ACLY induced an increase in apoptosis and a decrease in the migratory capacity of tumor cells and resulted in a decrease in the levels of acetyl coenzyme A, fatty acids, and cholesterol. However, the complexity of lipid metabolism increases the uncertainty of lipid-lowering therapies, and our study adds new possibilities for the anticancer effects of lipid metabolism inhibition, the complexity of which needs to be further explored in subsequent experiments. In addition, the reduction of lipid levels in tumor cells illustrates the possibility of ACLY inhibition to counteract DOX resistance, which suggests that ACLY could be a resistance target, but more evidence is needed to prove the relationship between the two. The reduction in lipid levels due to ACLY inhibition provides a theoretical basis for future studies, and we will continue to explore the extent and molecular mechanisms of the improvement in DOX resistance by ACLY inhibition to further refine the mechanism of action of multimodal synergistic therapy.

Many studies have been carried out in the last ten years to combine chemotherapy and photothermal therapy to improve chemotherapy resistance and treatment efficacy.[26] Since near-infrared light-mediated photothermal therapy is less invasive and has a high thermal ablation capacity, it has become a potent cancer treatment method. A wide range of nanomaterials have been created that, when they absorb near-infrared light, produce heat and serve as transporters for chemotherapeutic medications, thermal triggers for drug release, or thermotherapy-inducing synergistic effects.[19] The ultra-high specific surface area, low toxicity, and exceptional biocompatibility of graphene and its derivatives are well recognized. Furthermore, it has been demonstrated that graphene can intelligently and controllably transport a variety of compounds, including nucleic acids, proteins, and medications, into tumor cells in enormous quantities.[56] Compared to graphene, the oxidized form of graphene offers higher biocompatibility, good water solubility, and ease of functionalization. The kind and quantity of oxygen-containing functional groups can also be changed to alter the characteristics of graphene oxide. For example, adding more carboxyl groups greatly increases the material's water solubility, prevents agglomeration, and facilitates drug binding.[57] In this study, lipid-modulated nanoplatforms were synthesized using carboxylated graphene oxide loaded with SB-204990 and DOX. The morphology and structure of NSD were characterized by various means, and the particle size analysis showed that the entire particle size of NSD was <300 nm, which meets the size requirement of nanomaterials. The nanoplatform showed a high loading rate, pH and photothermal responsiveness, high photothermal conversion ability, and easy internalization by cells. Among them, the pH and photothermal responsiveness increased the effective concentration of anticancer drugs and improved the sensitivity of chemotherapeutic drugs thus better synergistic effects. Most importantly, both in vitro cytotoxicity and in vivo antitumor assays demonstrated that the NSD+Laser group showed a higher degree of tumor apoptosis than the monotherapy group, and even one nude mouse's tumor completely disappeared. The multimodal synergistic therapy of NSD demonstrated the optimal antitumor effect with low systemic toxicity. The anticancer strategies of NSD were analyzed:(1) ACLY inhibitors reduce the levels of various lipids in tumor cells, induce growth arrest, and have the potential to increase chemosensitivity. (2) NGO acted as a potent photothermal agent, mediating tumor ablation. (3) The pH response and photothermal response increased the effective intracellular concentration of SB-04990 and DOX and improved chemoresistance. (4) Lipid starvation, chemotherapy, and photothermal therapy act synergistically and mutually reinforce each other to maximize cancer inhibition.

We compared the relationship between resistance to chemotherapeutic agents commonly used in other studies and lipid metabolism. For example, Fluvastatin, a small-molecule inhibitor of hydroxymethylglutarate monoacyl-coenzyme A reductase (HMGR), the rate-limiting enzyme of the cholesterol synthesis process, was effective in combining with cisplatin to alleviate cisplatin resistance.[58] Oxaliplatin resistance can be counteracted by inhibiting lipid peroxidation in colorectal cancer treatment.[59] In addition, bevacizumab-induced extracellular matrix remodeling triggers lipid metabolic crosstalk between colon cancer cells and hepatic stellate cells, and this lipid metabolic crosstalk plays an important role in treatment resistance in patients with advanced colorectal tumors.[60] Our study raises the possibility that the reduction in lipid levels due to ACLY inhibition alleviates DOX resistance and that this reduction may be equally applicable to other chemotherapeutic agents, which inspires us to introduce

other chemotherapeutic agents into subsequent experiments in future studies to validate the generalizability of lipid-lowering therapies for chemo-sensitization strategies.

Although NSD nanoplatforms have shown significant therapeutic efficacy against OSCC in vivo and ex vivo experiments, approximately 15–30% of head and neck squamous cell carcinoma (HNSCC) patients still develop distant metastasis, which poses a challenge to local therapeutic strategies. In addition, tumor location and size limit effective drug delivery. To address these issues, we plan to explore the possibility of utilizing NSD nanoplatforms to achieve targeted therapy of OSCC in our subsequent studies, employing systemic administration for the treatment of the entire body, including primary and metastatic tumors, in order to improve the prognosis of OSCC patients. Meanwhile, although NSD nanoplatforms bring new hope for OSCC treatment with their efficient drug delivery, controlled release, and multimodal therapy, we also recognize that there is still a gap between experimental studies and clinical applications, and further efforts are needed to translate the research results into clinical treatments. How to translate novel nanoparticles into clinical applications is also the goal of our next phase of research.

In summary, it can be seen that our proposed new synergistic treatment strategy combining lipid starvation, chemotherapy, and photothermal therapy, while providing an effective treatment option for OSCC patients, also provides more theoretical support and experimental guidance for the application of nanocarrier-based multimodal synergistic therapy in the clinic, and demonstrates a wide range of application prospects.

Conclusion

In summary, we demonstrate that ACLY expression is upregulated in OSSC. Inhibition of ACLY resulted in increased apoptosis and decreased migration of tumor cells, as well as decreased levels of acetyl coenzyme A, fatty acids, and cholesterol, suggesting that ACLY will likely serve as a dual-action target for anticancer and improved chemotherapy tolerance. We synthesized a lipid-modulated nanoplatform (NSD) based on carboxylated graphene oxide, which enables synergistic treatment with lipid starvation, chemotherapy, and photothermal therapy. The NSD showed a high loading rate, pH and photothermal responsiveness, high photothermal conversion ability, and ease of internalization by cells. In vitro and in vivo trials have confirmed the significant synergistic effect of triple therapy compared to starvation therapy, chemotherapy, or photothermal therapy alone. Therefore, the NSD nanoplatform is a promising nanocarrier system for improving anti-tumor efficacy.

Abbreviations

NGO, nano-graphene oxide; DOX, doxorubicin; OSCC, oral squamous cell carcinoma; PTT, photothermal therapy; ACLY, ATP citrate lyase; FAO, fatty acid oxidation.

Acknowledgments

This study was supported by the 2023 Shanxi Provincial Higher Education General Teaching Reform and Innovation Project (J20230540), the Science and Technology Innovation Leader and Key Talent Team Project of Shanxi Province (202204051002034), Shanxi Province Science Popularization and Propaganda Special Project (2022060), Key Research and Development Projects of Shanxi Province (202302020101009), Scientific Research Topics of Shanxi Provincial Health and Wellness Committee(2023049), Graduate Student Research and Innovation Program of Shanxi Medical University (2023KY420), Central Guidance on Local Science and Technology Development Fund Projects (YDZJSX2024C029), Shanxi Clinical Medical Research Center Construction Project (202204010501006). The material in the picture of the animal experimental treatment process is from Scidraw.io.

Disclosure

The authors declare that they have no known competing financial interests or personal relationships that could have appeared to influence the work reported in this paper.

References

1. Sung H, Ferlay J, Siegel RL, et al. Global cancer statistics 2020: GLOBOCAN estimates of incidence and mortality worldwide for 36 cancers in 185 countries. *CA Cancer J Clin*. 2021;71(3):209–249. doi:10.3322/caac.21660

2. Tan Y, Wang Z, Xu M, et al. Oral squamous cell carcinomas: state of the field and emerging directions. *Int J Oral Sci*. 2023;15(1):44. doi:10.1038/s41368-023-00249-w
3. Yang M, Chen W, Gupta D, et al. Nanoparticle/engineered bacteria based triple-strategy delivery system for enhanced hepatocellular carcinoma cancer therapy. *Int J Nanomed*. 2024;19:3827–3846. doi:10.2147/IJN.S453709
4. Abdelmaksoud NM, Abulsoud AI, Doghish AS, Abdelghany TM. From resistance to resilience: uncovering chemotherapeutic resistance mechanisms; insights from established models. *Biochim Biophys Acta Rev Cancer*. 2023;1878(6):188993. doi:10.1016/j.bbcan.2023.188993
5. Zheng X, Song X, Zhu G, et al. Nanomedicine combats drug resistance in lung cancer. *Adv Mater*. 2024;36(3):e2308977. doi:10.1002/adma.202308977
6. Eslami M, Memarsadeghi O, Davarpanah A, Arti A, Nayernia K, Behnam BA-O. Overcoming chemotherapy resistance in metastatic cancer: a comprehensive review. *Biomedicines*. 2024;12:183. doi:10.3390/biomedicines12010183
7. Jin H-R, Wang J, Wang Z-J, et al. Lipid metabolic reprogramming in tumor microenvironment: from mechanisms to therapeutics. *J Hematol Oncol*. 2023;16(1):103. doi:10.1186/s13045-023-01498-2
8. Cheng Y-J, Fan F, Zhang Z, Zhang H-J. Lipid metabolism in malignant tumor brain metastasis: reprogramming and therapeutic potential. *Expert Opin Ther Targets*. 2023;27(9):861–878. doi:10.1080/14728222.2023.2255377
9. He M, Xu S, Yan F, Ruan J, Zhang X. Fatty acid metabolism: a new perspective in breast cancer precision therapy. *Front Biosci*. 2023;28(12):348. doi:10.31083/j.fbl2812348
10. Bacci M, Lorito N, Smiriglia A, Morandi A. Fat and furious: lipid metabolism in antitumoral therapy response and resistance. *Trends Cancer*. 2021;7(3):198–213. doi:10.1016/j.trecan.2020.10.004
11. Huang Q, Wang Q, Li D, et al. Co-administration of 20(S)-protopanaxatriol (g-PPT) and EGFR-TKI overcomes EGFR-TKI resistance by decreasing SCD1 induced lipid accumulation in non-small cell lung cancer. *J Exp Clin Cancer Res*. 2019;38(1):129. doi:10.1186/s13046-019-1120-4
12. He W, Liang B, Wang C, et al. MSC-regulated lncRNA MACC1-AS1 promotes stemness and chemoresistance through fatty acid oxidation in gastric cancer. *Oncogene*. 2019;38(23):4637–4654. doi:10.1038/s41388-019-0747-0
13. Kim D-H, Song N-Y, Yim H. Targeting dysregulated lipid metabolism in the tumor microenvironment. *Arch Pharm Res*. 2023;46(11–12):855–881. doi:10.1007/s12272-023-01473-y
14. Feng X, Zhang L, Xu S, Shen A-Z. ATP-citrate lyase (ACLY) in lipid metabolism and atherosclerosis: an updated review. *Prog Lipid Res*. 2020;77:101006. doi:10.1016/j.plipres.2019.101006
15. Guertin DA, Wellen KE. Acetyl-CoA metabolism in cancer. *Nat Rev Cancer*. 2023;23(3):156–172. doi:10.1038/s41568-022-00543-5
16. Zaidi N, Royaux I, Swinnen JV, Smans K. ATP citrate lyase knockdown induces growth arrest and apoptosis through different cell- and environment-dependent mechanisms. *Mol Cancer Ther*. 2012;11(9):1925–1935. doi:10.1158/1535-7163.MCT-12-0095
17. Liang -J-J, Zhou X-F, Long H, et al. Recent advance of ATP citrate lyase inhibitors for the treatment of cancer and related diseases. *Bioorg Chem*. 2024;142:106933. doi:10.1016/j.bioorg.2023.106933
18. Liu M, Zhang Z, Chen Y, Feng T, Zhou Q, Tian X. Circadian clock and lipid metabolism disorders: a potential therapeutic strategy for cancer. *Front Endocrinol*. 2023;14:1292011. doi:10.3389/fendo.2023.1292011
19. Li Z, Chen Y, Yang Y, et al. Recent advances in nanomaterials-based chemo-photothermal combination therapy for improving cancer treatment. *Front Bioeng Biotechnol*. 2019;7:293. doi:10.3389/fbioe.2019.00293
20. Sadeghi MS, Sangrizeh FH, Jahani N, et al. Graphene oxide nanoarchitectures in cancer therapy: drug and gene delivery, phototherapy, immunotherapy, and vaccine development. *Environ Res*. 2023;237(Pt 2):117027. doi:10.1016/j.envres.2023.117027
21. Li X, Wang Y, Liu T, Zhang Y, Wang C, Xie B. Ultrasmall graphene oxide for combination of enhanced chemotherapy and photothermal therapy of breast cancer. *Colloids Surf B Biointerfaces*. 2023;225:113288. doi:10.1016/j.colsurfb.2023.113288
22. Itoo AM, Vemula SL, Gupta MT, et al. Multifunctional graphene oxide nanoparticles for drug delivery in cancer. *J Control Release*. 2022;350:26–59. doi:10.1016/j.jconrel.2022.08.011
23. Uzdrowska K, Knap N, Gulczynski J, et al. Chasing graphene-based anticancer drugs: where are we now on the biomedical graphene roadmap? *Int J Nanomed*. 2024;19:3973–3989. doi:10.2147/IJN.S447397
24. Bellier N, Baipaywad P, Ryu N, Lee JY, Park H. Recent biomedical advancements in graphene oxide- and reduced graphene oxide-based nanocomposite nanocarriers. *Biomater Res*. 2022;26(1):65. doi:10.1186/s40824-022-00313-2
25. Li R, Liu C, Wan C, et al. A targeted and pH-responsive nano-graphene oxide nanoparticle loaded with doxorubicin for synergetic chemo-photothermal therapy of oral squamous cell carcinoma. *Int J Nanomed*. 2023;18:3309–3324. doi:10.2147/IJN.S402249
26. Husni P, Shin Y, Jeon H, et al. Development and characterization of pH-responsive nanocarriers for chemo-photothermal combination therapy of acidic tumors. *J Control Release*. 2023;359:52–68. doi:10.1016/j.jconrel.2023.05.025
27. Fan W, Peng H, Yu Z, et al. The long-circulating effect of pegylated nanoparticles revisited via simultaneous monitoring of both the drug payloads and nanocarriers. *Acta Pharm Sin B*. 2022;12(5):2479–2493. doi:10.1016/j.apsb.2021.11.016
28. Zeng W, Luo Y, Gan D, Zhang Y, Deng H, Liu G. Advances in doxorubicin-based nano-drug delivery system in triple negative breast cancer. *Front Bioeng Biotechnol*. 2023;11:1271420. doi:10.3389/fbioe.2023.1271420
29. Almajidi YQ, Kadhim MM, Alsaikhan F, et al. Doxorubicin-loaded micelles in tumor cell-specific chemotherapy. *Environ Res*. 2023;227:115722. doi:10.1016/j.envres.2023.115722
30. Ibrahim AA, Nsairat H, Al-Sulaibi M, et al. Doxorubicin conjugates: a practical approach for its cardiotoxicity alleviation. *Expert Opin Drug Deliv*. 2024;21(3):399–422. doi:10.1080/17425247.2024.2343882
31. Sun H, Wang F, Huang Y, et al. Targeted inhibition of ACLY expression to reverse the resistance of sorafenib in hepatocellular carcinoma. *J Cancer*. 2022;13(3):951–964. doi:10.7150/jca.52778
32. He R, Yang P, Liu A, et al. Cascade strategy for glucose oxidase-based synergistic cancer therapy using nanomaterials. *J Mater Chem B*. 2023;11(41):9798–9839. doi:10.1039/d3tb01325a
33. Li R, Wan C, Li Y, et al. Nanocarrier-based drug delivery system with dual targeting and NIR/pH response for synergistic treatment of oral squamous cell carcinoma. *Colloids Surfaces B*. 2024;244:114179. doi:10.1016/j.colsurfb.2024.114179
34. Chen Y, Li K, Gong D, et al. ACLY: a biomarker of recurrence in breast cancer. *Pathol Res Pract*. 2020;216(9):153076. doi:10.1016/j.prp.2020.153076

35. Migita T, Narita T, Nomura K, et al. ATP citrate lyase: activation and therapeutic implications in non-small cell lung cancer. *Cancer Res*. 2008;68 (20):8547–8554. doi:10.1158/0008-5472.CAN-08-1235
36. Cui Y, Man S, Tao J, et al. The lipid droplet in cancer: from being a tumor-supporting hallmark to clinical therapy. *Acta Physiol*. 2024;240(3): e14087. doi:10.1111/apha.14087
37. Zhang X, Xu Y, Li S, et al. SIRT2-mediated deacetylation of ACLY promotes the progression of oesophageal squamous cell carcinoma. *J Cell Mol Med*. 2024;28(6):e18129. doi:10.1111/jcmm.18129
38. Singh KB, Hahm E-R, Kim S-H, Singh SV. Withaferin A inhibits fatty acid synthesis in rat mammary tumors. *Cancer Prev Res*. 2023;16(1):5–16. doi:10.1158/1940-6207.CAPR-22-0193
39. Khwairakpam AD, Shyamananda MS, Sailo BL, et al. ATP citrate lyase (ACLY): a promising target for cancer prevention and treatment. *Curr Drug Targets*. 2015;16(2):156–163. doi:10.2174/1389450115666141224125117
40. He W, Li Q, Li X. Acetyl-CoA regulates lipid metabolism and histone acetylation modification in cancer. *Biochim Biophys Acta Rev Cancer*. 2023;1878(1):188837. doi:10.1016/j.bbcan.2022.188837
41. Yan X, Zhao X, Fan M, et al. Acidic environment-responsive metal organic framework-mediated dihydroartemisinin delivery for triggering production of reactive oxygen species in drug-resistant lung cancer. *Int J Nanomed*. 2024;19:3847–3859. doi:10.2147/IJN.S451042
42. Chen Z, Wang X, Zhao N, Chen H, Guo G. Advancements in pH-responsive nanocarriers: enhancing drug delivery for tumor therapy. *Expert Opin Drug Deliv*. 2023;20(11):1623–1642. doi:10.1080/17425247.2023.2292678
43. Castelló CM, de Carvalho MT, Bakuzis AF, Fonseca SG, Miguel MP. Local tumour nanoparticle thermal therapy: a promising immunomodulatory treatment for canine cancer. *Vet Comp Oncol*. 2022;20(4):752–766. doi:10.1111/vco.12842
44. Paramo L, Jiménez-Chávez A, Medina-Ramirez IE, Böhnel HN, Escobar-Alarcón L, Esquivel K. Biocompatibility evaluation of TiO2, Fe3O4, and TiO2/ Fe3O4 nanomaterials: insights into potential toxic effects in erythrocytes and HepG2 cells. *Nanomaterials*. 2023;13(21):2824. doi:10.3390/nano13212824
45. Li Y, Hou H, Liu Z, et al. CD44 targeting nanodrug based on chondroitin sulfate for melanoma therapy by inducing mitochondrial apoptosis pathways. *Carbohydr Polym*. 2023;320:121255. doi:10.1016/j.carbpol.2023.121255
46. Dash BS, Lu Y-J, Chen H-A, Chuang -C-C, Chen J-P. Magnetic and GRPR-targeted reduced graphene oxide/doxorubicin nanocomposite for dual-targeted chemo-photothermal cancer therapy. *Mater Sci Eng C Mater Biol Appl*. 2021;128:112311. doi:10.1016/j.msec.2021.112311
47. Zhang L, Qin Y, Zhang Z, et al. Dual pH/reduction-responsive hybrid polymeric micelles for targeted chemo-photothermal combination therapy. *Acta Biomater*. 2018;75:371–385. doi:10.1016/j.actbio.2018.05.026
48. Miao X, Wang B, Chen K, et al. Perspectives of lipid metabolism reprogramming in head and neck squamous cell carcinoma: an overview. *Front Oncol*. 2022;12:1008361. doi:10.3389/fonc.2022.1008361
49. Shi E, Shan T, Wang H, et al. A bacterial nanomedicine combines photodynamic-immunotherapy and chemotherapy for enhanced treatment of oral squamous cell carcinoma. *Small*. 2023;19(52):e2304014. doi:10.1002/smll.202304014
50. Fang K, Sun M, Leng Z, et al. Targeting IGF1R signaling enhances the sensitivity of cisplatin by inhibiting proline and arginine metabolism in oesophageal squamous cell carcinoma under hypoxia. *J Exp Clin Cancer Res*. 2023;42(1):73. doi:10.1186/s13046-023-02623-2
51. Jin H, Wang L, Bernards R. Rational combinations of targeted cancer therapies: background, advances and challenges. *Nat Rev Drug Discov*. 2023;22(3):213–234. doi:10.1038/s41573-022-00615-z
52. Jiao R, Jiang W, Xu K, Luo Q, Wang L, Zhao C. Lipid metabolism analysis in esophageal cancer and associated drug discovery. *J Pharm Anal*. 2024;14(1):1–15. doi:10.1016/j.jpha.2023.08.019
53. Li C, Wang F, Cui L, Li S, Zhao J, Liao L. Association between abnormal lipid metabolism and tumor. *Front Endocrinol*. 2023;14:1134154. doi:10.3389/fendo.2023.1134154
54. Wang Z, Wang Y, Li Z, Xue W, Hu S, Kong X. Lipid metabolism as a target for cancer drug resistance: progress and prospects. *Front Pharmacol*. 2023;14:1274335. doi:10.3389/fphar.2023.1274335
55. Wen J, Min X, Shen M, et al. ACLY facilitates colon cancer cell metastasis by CTNNB1. *J Exp Clin Cancer Res*. 2019;38(1):401. doi:10.1186/ s13046-019-1391-9
56. Borzooee Moghadam N, Avatefi M, Karimi M, Mahmoudifard M. Graphene family in cancer therapy: recent progress in cancer gene/drug delivery applications. *J Mater Chem B*. 2023;11(12):2568–2613. doi:10.1039/d2tb01858f
57. Barjola A, Tormo-Mas MÁ, Sahuquillo O, Bernabé-Quispe P, Pérez JM, Giménez E. Enhanced antibacterial activity through silver nanoparticles deposited onto carboxylated graphene oxide surface. *Nanomaterials*. 2022;12(12):1949. doi:10.3390/nano12121949
58. Bi YY, Chen Q, Yang MY, Xing L, Jiang HA-O. Nanoparticles targeting mutant p53 overcome chemoresistance and tumor recurrence in non-small cell lung cancer. *Nat Commun*. 2024;15. 2759. doi:10.1038/s41467-024-47080-3
59. Zeng K, Li W, Wang Y, et al. Inhibition of CDK1 overcomes oxaliplatin resistance by regulating ACSL4-mediated ferroptosis in colorectal cancer. *Adv Sci*. 2023;10: 2301088. doi:10.1002/advs.202301088.
60. Zheng YA-O, Zhou RA-O, Cai JA-O, et al. Matrix stiffness triggers lipid metabolic cross-talk between tumor and stromal cells to mediate bevacizumab resistance in colorectal cancer liver metastases. *Cancer Res*. 2023;83(21):3577–92 doi:10.1158/0008-5472.CAN-23-0025..